

The Missing Link: Au₁₉₁(SPh-*t*Bu)₆₆ Janus Nanoparticle with Molecular and Bulk-Metal-like Properties

Naga Arjun Sakthivel, Masoud Shabaninezhad, Luca Sementa, Bokwon Yoon, Mauro Stener, Robert L. Whetten, Guda Ramakrishna, Alessandro Fortunelli, Uzi Landman, and Amala Dass*

Cite This: *J. Am. Chem. Soc.* 2020, 142, 15799–15814

Read Online

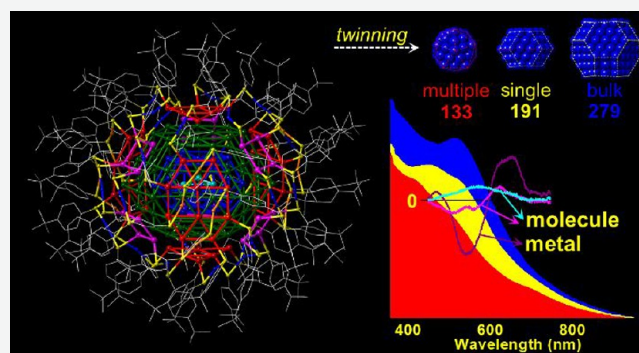
ACCESS |

Metrics & More

Article Recommendations

Supporting Information

ABSTRACT: Understanding the evolution of the structure and properties in metals from molecule-like to bulk-like has been a long sought fundamental question in science, since Faraday's 1857 work. We report the discovery of a Janus nanomolecule, Au₁₉₁(SPh-*t*Bu)₆₆ having both molecular and metallic characteristics, explored crystallographically and optically and modeled theoretically. Au₁₉₁ has an anisotropic, singly twinned structure with an Au₁₅₅ core protected by a ligand shell made of 24 monomeric [–S–Au–S–] and 6 dimeric [–S–Au–S–Au–S–] staples. The Au₁₅₅ core is composed of an 89-atom inner core and 66 surface atoms, arranged as [Au₃@Au₂₃@Au₆₃]@Au₆₆ concentric shells of atoms. The inner core has a monotwinned/stacking-faulted face-centered-cubic (fcc) structure. Structural evolution in metal nanoparticles has been known to progress from multiply twinned, icosahedral, structures in smaller molecular sizes to untwinned bulk-like fcc monocrystalline nanostructures in larger nanoparticles. The monotwinned inner core structure of the ligand capped Au₁₉₁ nanomolecule provides the critical missing link, and bridges the size-evolution gap between the molecular multiple-twinning regime and the bulk-metal-like particles with untwinned fcc structure. The Janus nature of the nanoparticle is demonstrated by its optical and electronic properties, with metal-like electron–phonon relaxation and molecule-like long-lived excited states. First-principles theoretical explorations of the electronic structure uncovered electronic stabilization through the opening of a shell-closing gap at the top of the occupied manifold of the delocalized electronic superatom spectrum of the inner core. The electronic stabilization together with the inner core geometric stability and the optimally stapled ligand-capping anchor and secure the stability of the entire nanomolecule.



INTRODUCTION

The evolution of the transition in properties of metallic particles from being molecular in nature to exhibiting bulk-metal characteristics has been a rich source of scientific debate and discussion since the seminal work of Michael Faraday in 1857, where he concluded that “the ruby gold behaves exactly as metallic gold” and wondered whether these particles are “molecules of gold”.¹ The development of a facile protocol² for the synthesis of thiolate protected gold nanoparticles (AuNPs) and the discovery³ of the manifestation of a discrete, molecular-like, size-dependent evolution^{3,4} of their properties^{3,4} have led to atomically precise determination⁵ of their structures with tens to hundreds of metal atoms.^{5–15} These developments have advanced the understanding of their self-assembly, structure, and properties, as well as that of superstructures made of them as elemental building blocks, and resulted in the advancement of methods and strategies for further development and their application.^{14,16–26} The size-dependent structure and property evolution of nanomolecules provides the opportunity to understand the fundamental

nature of matter and the principles governing its evolution with size.^{3,7,27–46} However, although significant information and insights have been gained over the past two and a half decades from queries pertaining to “how and where” size-evolutionary changes in materials’ properties occur, in the sense of explorations of the mechanisms and processes by which materials’ properties change with the degree of aggregation and at what sizes such transitions exhibit themselves, many aspects of this problem remain open.

Following the early introduction of a facile procedure for thiolate-capped AuNPs synthesis,² and the pioneering combined experimental and theoretical characterization of such gold nanomolecules (AuNMs), described as “...perfect

Received: May 25, 2020

Published: September 3, 2020



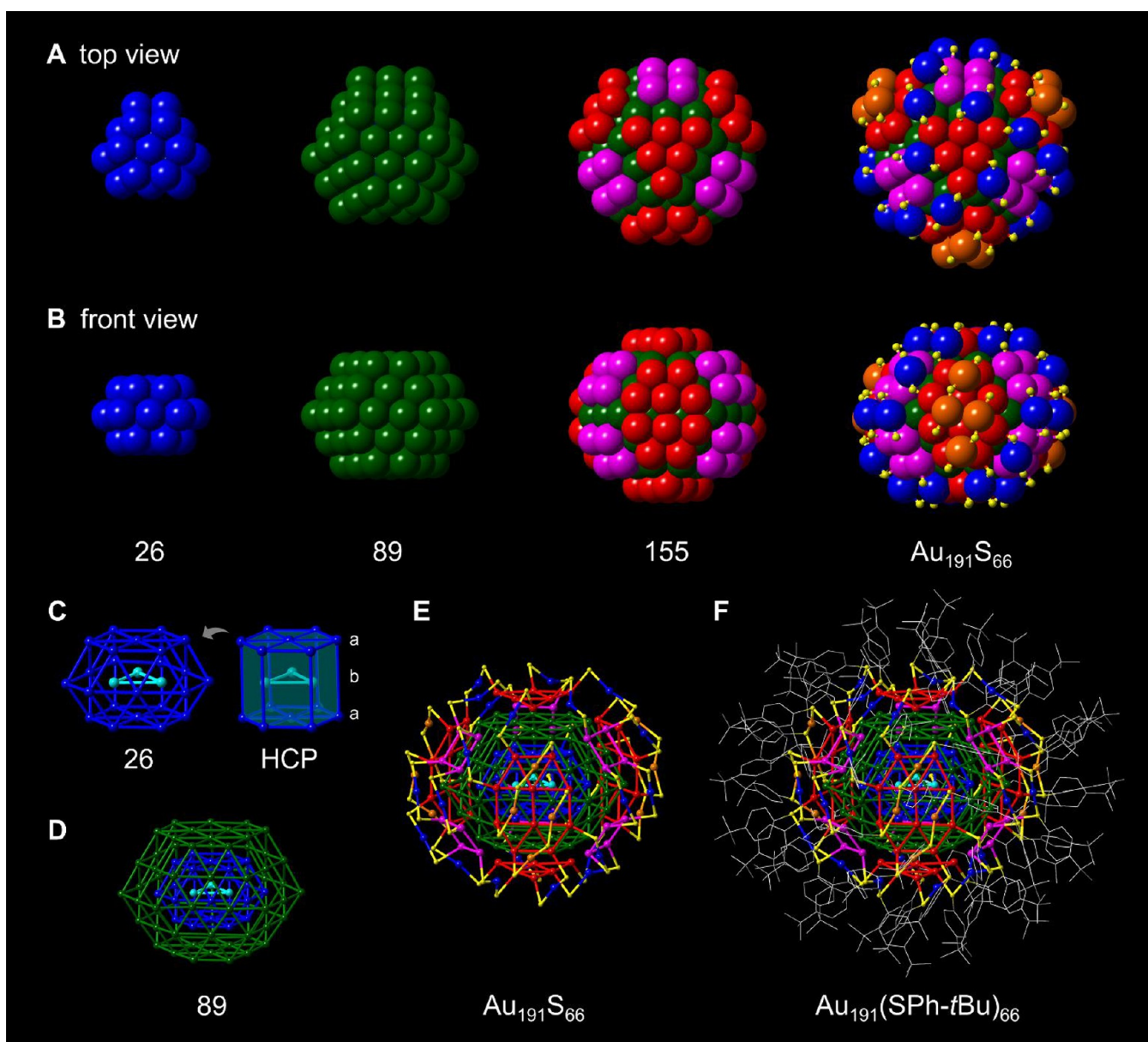


Figure 1. X-ray crystal structure of the anisotropic $\text{Au}_{191}(\text{SPh-}t\text{Bu})_{66}$ nanomolecules. (A) Top and (B) front views (from left to right): (i) the HCP Au_{26} kernel, located inside the inner core; (ii) the entire Au_{89} inner core; (iii) the Au_{155} core cluster, that is, the 89-atom inner core with the 66-atom surface thiolate ligand-anchoring pads; the facets of the Au_{155} cluster are displayed as red, $\{111\}$ facets; magenta, $\{100\}$ facets; and (iv) the left-most configuration in (A) and (B) that displays the entire thiol-protected nanoparticle, with only the sulfur atoms shown (small yellow balls). Note that (A) shows a twin domain viewed along the C_3 axis (the perpendicular mirror plane lies in the plane of the paper). Part (B) is viewed along a C_2 axis. (C) Classic HCP unit cell embedded in the Au_{26} kernel. Core-shell view of (D) the inner core, (E) $\text{Au}_{191}\text{S}_{66}$, and (F) $\text{Au}_{191}(\text{SPh-}t\text{Bu})_{66}$ (gray, C). Intershell linkages and hydrogen atoms are excluded for clarity. The color designations are as follows: center Au_3 atoms, cyan; Au_{23} , blue; Au_{63} , olive; S, yellow; and staple motifs, blue, monomeric Au; orange, dimeric Au.

nanometer-scale crystallites (nanocrystals), identically replicated in unlimited quantities, in a state that can be manipulated and understood as pure macromolecular substances, is an ultimate challenge of modern materials research with outstanding fundamental and potential technological consequences³; the large majority of studies on the size-evolution of metal nanoparticles have been carried out using gold as the metal being probed, with a variety of organic ligands as capping agents. Each ligand type results in a distinct series of AuNMs sizes and properties.⁴⁷ We focus here on AuNMs of variable sizes, all capped by 4-*tert*-butylbenzenethiolate (SPh-*t*Bu, TBBT) ligand. The plethora of AuNMs

structural motifs and the size-dependent variability of their chemical and physical properties probed with the use of a broad spectrum of experimental and theoretical methodologies, including X-ray crystallography,⁷ electron microscopy,³ optical spectroscopy,^{27,40,46} electrochemical measurements,^{20,28,33,48} and chemical activity and catalytic reactivity,^{26,49} have indeed identified these systems as ones characterized by superior stability, which exhibit readily observable quantum confinement effects in the 1–3 nm size range. These characteristics have positioned AuNMs as favorable systems for serving as a test bed for the exploration

and understanding of the physical origins of the underlying materials' structure and property evolution with size.

A series of TBBT-capped AuNMs containing a sequence of sizes, ranging from 10 to 279 gold atoms, have been studied, of which Au₁₃₃ and Au₂₇₉ mark the size-boundaries, characterized by molecule-like (quantized discrete electronic structure) at the lower boundary (Au₁₃₃) and as metallic (plasmonic) in nature at the higher end (Au₂₇₉), with no other TBBT-capped AuNMs characterized between these sizes.^{7,31,32,50–58} Au₁₃₃(TBBT)₅₂ has a compact Mackay-icosahedral (*I_h*) 55-site core structure, regarded as a multiply twinned variant of the 55-site fcc (cuboctahedral, CO) nanocrystallite. The essential electronic (and optical) character of Au₁₃₃(TBBT)₅₂ is nonplasmonic (nonmetallic).³¹ A series of smaller homologues are “cuboidal” in morphology and even less bulk-like.⁷ In the latter case of Au₂₇₉(TBBT)₈₄, the core is a regular 147-site nanocrystallite, recognized as an fcc cuboctahedron or alternatively as a 201-site fcc truncated octahedron (TO), also referred to as “Wulff polyhedron” morphology of fcc metals, with 8 {111} facets and 6 {100} facets. The electronic, electrodynamic (spectroscopic), and electrochemical properties of Au₂₇₉ are essentially plasmonic (metallic).⁵⁹ Clearly, there is a large gulf, not only in size (~27 kDa Au₁₃₃ vs ~54 kDa Au₂₇₉ by mass) but also in essential physical character, that separates the largely “molecular” (in the sense of nonbulk) character of the Au₁₃₃(TBBT)₅₂ nanomolecule from the evidently “metallic” (in the sense of bulk-like) character of the larger Au₂₇₉(TBBT)₈₄.

Despite some early hints that dated back to the first indication of nanocrystal gold molecules of ~38 kDa in core mass,⁶⁰ there has been no resolution offered yet to the evermore vexing leap in the size-evolution, the structural motif transformation from extreme multiple-twinning (*I_h*) to single-crystalline truncated-octahedral cores, as well as the transition from nonmetallic to characteristic metallic (plasmonic) properties of the optoelectronic response. The composition of the aliphatic thiolate-protected ~38 kDa core compound was found to be Au₁₈₇(SR)₆₈,^{60–62} and (judging from its optical response) it lies in the transition region between the molecule-like Au₁₄₄(SR)₆₀ and the plasmonic Au₃₂₉(SR)₈₄ NM, which also belongs to the aliphatic thiolate-capped series.^{30,63} The Au₁₈₇(SR)₆₈ nanomolecule has not been crystallographically studied to date, and the optical properties are yet to be explored in detail.

Here, we address the above-noted outstanding open question pertaining to the “missing-link” TBBT-capped Au₁₉₁ AuNP whose size is intermediary between Au₁₃₃ and Au₂₇₉ nanomolecules. To this end, we have engineered the synthesis of a nanomolecule with 191 Au atoms and 66 TBBT ligands, found to exhibit hybrid structural and electronic properties. A crude product of AuNPs was synthesized, thermochemically etched with excess TBBT ligands, and a molecularly pure Au₁₉₁ product was isolated by size exclusion chromatography; see the Supporting Information for details.^{31,32} The composition and purity were verified by mass spectrometry (see below). The product has a molecular weight of 48 528.8 Da. The Au₁₉₁(SPh-*t*Bu)₆₆ crystals were grown by slow evaporation and studied by single-crystal X-ray diffraction (SC-XRD). Steady-state and transient absorption (TA) spectroscopy and time-dependent density functional theory (TDDFT) simulations were performed to shed light on the intermediate molecular/metallic nature of the optical properties and

electronic structure (refer to the Supporting Information for detailed methods).

The electronic origins of the energetic stability that characterizes the “missing-link” TBBT-capped 191-atom AuNM were gained through the analysis of the first-principle calculated electronic spectrum (through analysis of a generalization of the electronic cluster-shell model (CSM),⁶⁴ termed recently⁵⁴ as the core-CSM (or CCSM)). Indeed, the electronic spectrum of the Au₁₉₁ inner core exhibits a superatom shell structure with a shell-closing stabilization gap of 0.42 eV, and the crystallographic structure of the inner core reveals a monotwinned *D_{3h}* stacking-faulted fcc crystallite, which provides the long-sought-after missing-link bridge between the multiply twinned Au₁₃₃(TBBT)₅₂ and monocrystalline Au₂₇₉(TBBT)₈₄ nanomolecules.

RESULTS AND DISCUSSION

Au₁₉₁(SPh-*t*Bu)₆₆ Nanomolecule Superlattice Crystal Structure. The X-ray-determined superlattice of the Au₁₉₁ nanomolecule self-assembles in layers on the *xy*-plane, stacked with alternate layers of enantiomers along the *z*-axis in a 1:1 ratio, with each nanomolecule having six nearest neighbors (Figures S1 and S2). Each AuNM has four neighbors in the *xy*-plane and one neighbor in each of the two adjacent planes, with center-to-center interparticle distances of 3.2 and 3.22 nm, respectively. Two AuNMs (enantiomers) are located in the middle of the unit cell, and their corresponding four neighbors are situated on the four *c* edges, with each shared by four neighboring unit cells (8/4), which leads to a total contribution of four AuNMs per unit cell.

Au₁₉₁(SPh-*t*Bu)₆₆ Nanomolecule Crystal Structure. The X-ray crystal structure was solved in the *C2/c* space group at 1.15 Å resolution to a reliability (residual) factor *R*₁ = 5.7% (Table S1). The Au₁₉₁ nanomolecule has an anisotropic, monotwinned structure with an approximate dimension of 3.4 nm × 3.2 nm (Figures 1 and S3). The nanomolecule is composed of three major parts: an inner core, surface anchoring pads, and a ligand shell. The inner core is made of 89 gold atoms that are devoid of any direct bonding to the capping thiolate ligands (Figure 1). It has a core–shell structure with a 26-atom hexagonal close packed (HCP) kernel, encapsulated by a 63-Au-atom shell. The classic HCP unit cell can be found embedded in the 26-atom kernel (Figure 1C). Such an Au₂₆ kernel has been computationally identified to be one of the most stable close-packed structures.^{65,66}

The 89-atom inner core is a 14 faceted convex polyhedron with 18 vertices and 30 edges (Figure S4). The 14 facets can be further classified as eight {111} and six {100} facets. The hexagonal and trapezoidal shapes form the {111} facets, and the {100} facets are square-shaped. In total, there are two hexagonal, six trapezoidal, and six square facets. The hexagonal facets form the poles, along the principal three-fold rotational axis. Three square and three trapezoidal facets then are arranged in an alternating fashion while sharing their edges and legs (Figure S4). The equatorial mirror plane mirrors that arrangement to form a convex polyhedron. There are three perpendicular two-fold rotational axes located along the equatorial plane. Overall, the inner core has a *D_{3h}* symmetry. It provides a perfect template for the surface anchoring pads (66 gold-sites). The anchoring pads are distributed as 6-atom triangular {111} facets on the poles, 5-atom trapezoidal {111} facets, and 4-atom square {100} facets on the body. The Au₁₅₅ core retains the *D_{3h}* symmetry (Figure 1).

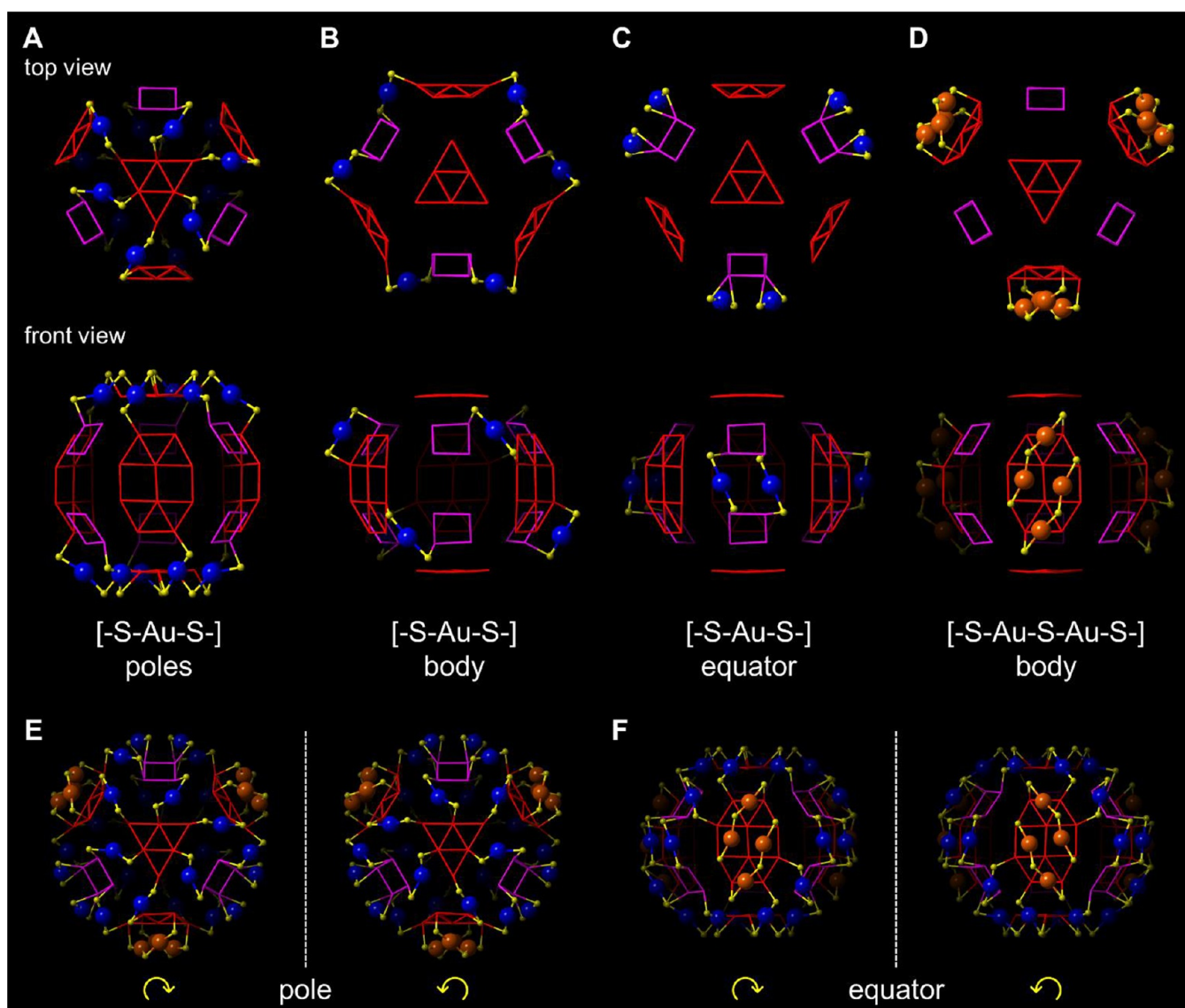


Figure 2. Staple motif assembly on Au_{191} . Monomeric staples on (A) poles, (B) body, and (C) the equatorial position. (D) Dimeric staples solely located on the trapezoidal $\{111\}$ facets. Staple motif assemblies in the enantiomers of Au_{191} are shown in (E) and (F), viewed in (E) along the C_3 axis through the poles and in (F) along the C_2 axis through the equatorial position. Color designations are followed as in Figure 1. The Au_{89} inner core and C, H are excluded for brevity.

Ligand Shell. The ligand shell is made of staple motifs with 36 gold sites and a thiolate monolayer with 66 TBBT ligands. The staple motifs protect the Au_{155} surface atoms and the re-entrant grooves between the surface facets. The staples are of two kinds: monomeric ($-\text{S}-\text{Au}-\text{S}-$) and dimeric ($-\text{S}-\text{Au}-\text{S}-\text{Au}-\text{S}-$) staples, and there are 24 monomeric and 6 dimeric staples (Figures 1, 2, and S5). In the staples, the $\text{Au}-\text{S}-\text{Au}$ angles range from 71.1° to 118.3° , and the $\text{S}-\text{Au}-\text{S}$ angles range from 138.7° to 173.2° .

Distribution of the Staple Motifs. The staple motifs protect the nanocrystallite surface in a structural and energetic optimal interfacet configuration. The monomeric staples are distributed in three areas: 6 per pole, 6 on body, and 6 on the equatorial positions. (i) The poles have 6-atom triangular facets, which are protected by 6 monomeric staples (Figure 2A). The monomeric staples from atoms on a triangular $\{111\}$ facet's vertices anchor a vertex atom on a trapezoidal $\{111\}$ facet. The monomeric staples from atoms on a triangular $\{111\}$ facet's edges anchor a vertex atom on square $\{100\}$

facets. The staple motif assembly on the poles of the Au_{191} is very similar to the case of the Au_{279} nanomolecule.³² (ii) On the body, the monomeric staples from an atom on the square $\{100\}$ facet anchor a vertex atom on trapezoidal $\{111\}$ facets (Figure 2B). (iii) At the equatorial position, the monomeric staples from the remaining two atoms on a square $\{100\}$ facet on one-half of the body protect the remaining two atoms on the square $\{100\}$ facet (on the other one-half of the body) across the equatorial mirror plane (Figure 2C).

The dimeric staples are solely located on the trapezoidal facets. The monomeric staples protect two of the five atoms in the trapezoidal facet. Two of the remaining three atoms on the trapezoidal facets are protected by one end of the dimeric (long) staples, and the other end protects the two atoms on the trapezoidal facet across the equatorial mirror plane. One atom at the base of each trapezoidal facet remains without any interaction with the thiolate group, as it is buried under the dimeric staple metal atoms (Figure 2D). The thiolate monolayer retains only the (three-fold and two-fold) rotational

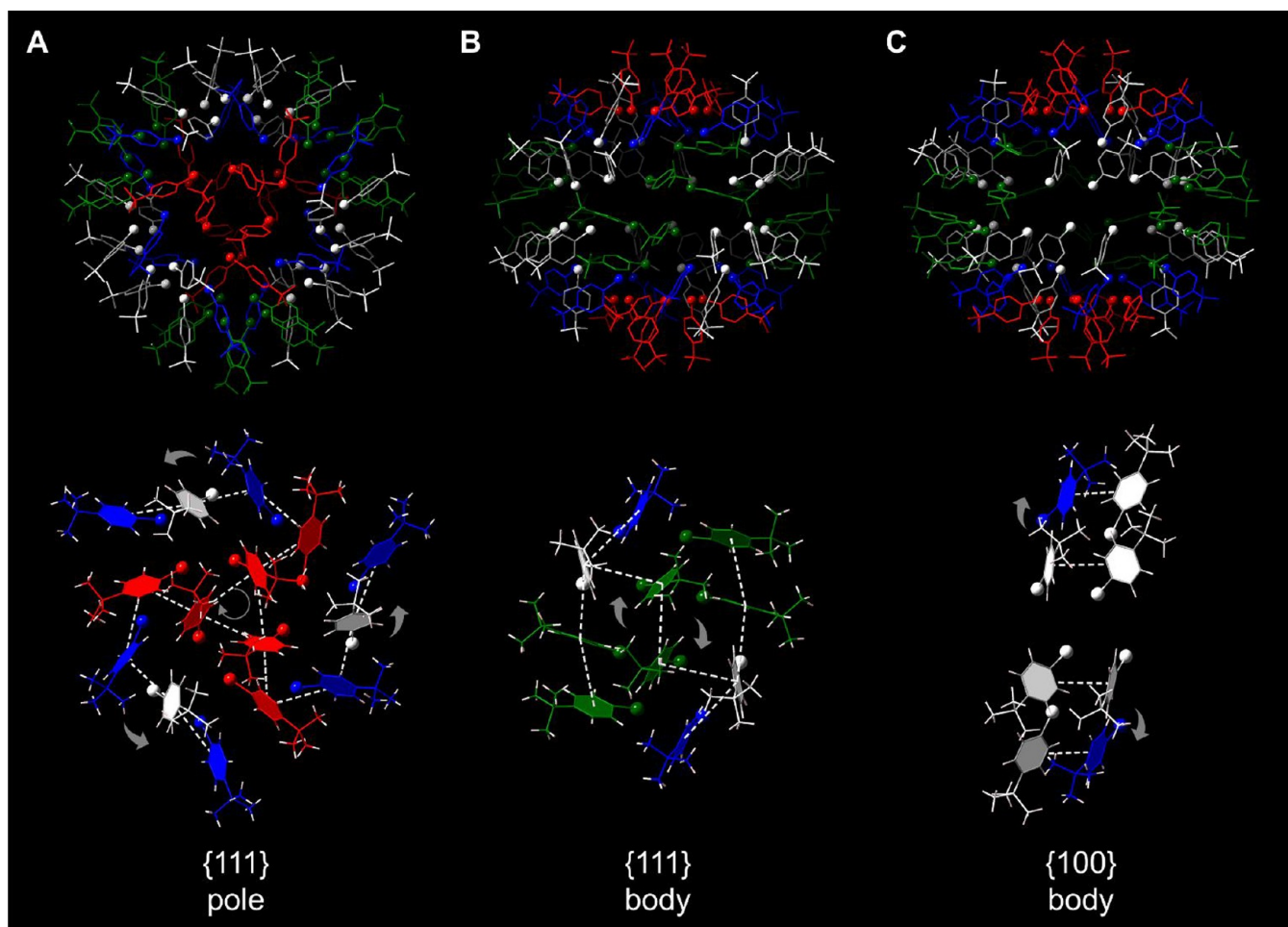


Figure 3. TBBT monolayer on $\text{Au}_{191}(\text{SPh-}t\text{Bu})_{66}$. Thiolate monolayer assembly on the $\text{Au}_{191}(\text{SPh-}t\text{Bu})_{66}$ nanocrystal viewed along (A) the three-fold axis perpendicular to the pole $\{111\}$ facet, and the two-fold axis at the equatorial position through (B) dimeric staples on the body $\{111\}$ facet and (C) monomeric staples on the $\{100\}$ facets. Hydrogens are excluded for clarity. The second row of frames reveals the thiolate monolayer assembly on specific facets (dashed lines, interligand phenyl–phenyl interactions; the arrows indicate the direction of rotation). Ligands are color coded as follows: red, poles; blue, monomeric staple ligands extending out of the poles; olive, dimeric staples; and white, monomeric staples on the $\{100\}$ facets.

axes and breaks the symmetry to a chiral D_3 symmetry. Figure 2E,F displays the staple motif assembly on the enantiomers of Au_{191} nanomolecule.

Thiolate Monolayer Assembly. The ligand shell is stabilized by staple Au–S interactions, as well as interligand (phenyl–phenyl(π – π), CH– π , and S– π) and Au– π interactions. The interligand interaction distance ranges are CH– π , 2.4–3.1 Å; S– π , 3.6–4.3 Å; Au– π , 3.4–4.4 Å; and π – π , 4.3–5.5 Å. The interligand interactions run from pole to pole and along the body. The interligand phenyl–phenyl interactions resemble the triskelion-like motifs on the poles, like a clathrin lattice⁶⁷ (Figures 3 and S6). The three arms extending from the triskelion run down through the long staples on the body and meet the arms extending from the other pole. The interligand interactions on each half of the body run parallel to the directionality of the triskelion-like motifs’ arms (Figures 3 and S6).

Parentage of the D_{3h} - Au_{89} Inner Core. The identification of the stable convex D_{3h} - Au_{89} polyhedral kernel, as the “inner core” of the Au_{191} nanoparticle, came as a welcome surprise, particularly at this late stage of development of our understanding of the nanoparticles’ structural motifs, a topic that has been preoccupying researchers in this field for close to

three decades.⁶⁸ The detailed analysis of its construction (Figure 4) and interatomic distances (Figure 5), either as concentric shells of atoms (Figures S7 and S8, and Table S2) or in a layer-by-layer fashion along its principal symmetry axis, suffices to reveal many similarities, as well as key differences, with respect to bulk fcc gold as well as structures of large or small AuNMs. Additionally, there is little or no hint of any strain in the structure.

Of further interest is the parentage of the inner core D_{3h} - Au_{89} polyhedron, as an fcc twin, to the nearest Wulff⁶⁹ polyhedral structure, TO-116 (Figure 4). Unlike the straightforward analysis of the kernel in the $\text{Au}_{146}(\text{SR})_{57}$ structure,⁷⁰ which is a twinned form of the well-known TO-79 nanocrystallite (or a twinned cuboctahedral-55 inner core), the analysis of the D_{3h} - Au_{89} parentage appears to be more intricate.

In the untwinned TO-116 structure, along any three-fold (C_3) axis, the $\{111\}$ planes are ordered (stacked) as $\{abcabc\}$, as for any six-layer untwinned fcc structure (Figure 4B). The number of sites in each layer of TO-116 is $\{12:19:27:27:19:12\}$, similar to the five-layer $\{abcba\} = \{12:19:27:19:12\}$ of the D_{3h} - Au_{89} kernel (Figure 4A,B). The former may be converted to the latter in two steps: (i) first, a

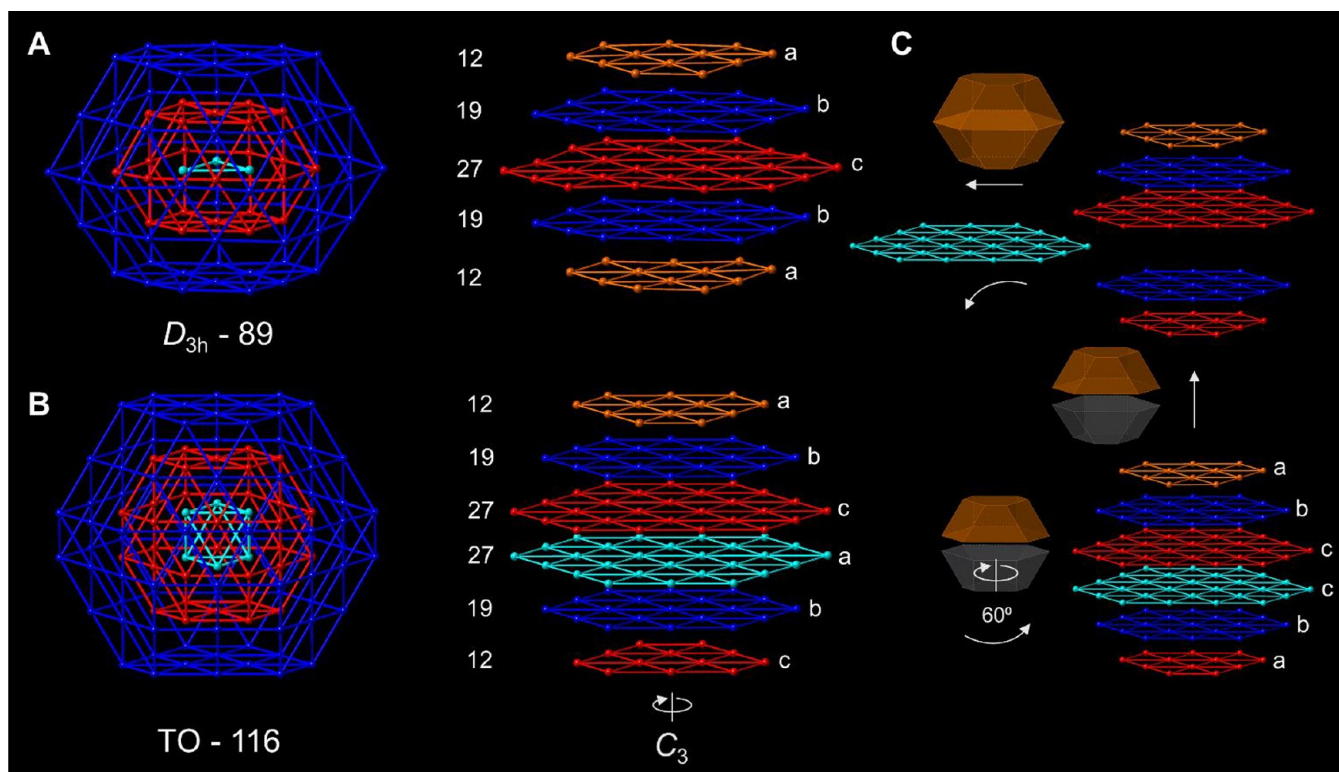


Figure 4. Parentage of the D_{3h} 89-atom inner core. (A) The arrangement of gold atoms along the three-fold axis of the monotwinned fcc D_{3h} 89-atom core. (B) Untwinned TO-116. Core–shell depiction in the left column, with the corresponding layer-stacking along the C_3 axis shown in the middle column. (C) Transformation from TO-116 (B) to the monotwinned fcc D_{3h} 89-atom inner core (A). Core–shell color code: cyan, core center atoms; red, first shell; blue, outer shell.

twinning operation is performed by fixing the upper half and then rotating the lower half by 60° around the three-fold axis, but with the unusual feature that the twinning plane lies between the two middle planes of 27 atoms each, rather than coinciding with one of these planes (Figure 4C). The layer-stacking sequence becomes $\{abcba\}$; that is, it introduces a mirror plane, at the cost of introducing a c – c fault junction. In a subsequent step, (ii) one of the c -planes is removed. The remaining c -layer becomes a reflecting plane in the new sequence of $\{abcba\} = \{12:19:27:19:12\}$. Twinned TO structures generally exhibit re-entrant (concave) features, whereas the procedure just described produces a convex form. It is apparent that this high-stability crystallographic structure has been missed in the earlier database literature on clusters' nanocrystalline motifs.

Alternatively, the 89-atom inner core can be viewed as three fused anticuboctahedra (also known as Johnson solid J27);⁷¹ however, three-fused cuboctahedra have only 86 atoms (Figure S9). Therefore, it is not possible to achieve the D_{3h} -Au₈₉ by rotating one-half of the 86-atom polyhedra by 60° along the principal C_3 rotational axis. Au₂₇₉ has a classic 7-layer fcc stacking arrangement along any three-fold axis in TO-201, with the $\{111\}$ planes ordered as $\{abcabcba\} = \{19:27:36:37:36:27:19\}$ (Figure S9).

Transition from Multiply Twinned Au₁₃₃ to Monotwinned Au₁₉₁ to Untwinned Bulk-like Au₂₇₉. Structural evolution in metal NPs has been studied over the last several decades to understand the evolution of matter as a function of size.^{68,72–79} The discovery of Au₁₉₁ in the TBBT-capped AuNMs series⁷ reveals that, indeed, the structure evolves from multiply twinned, icosahedral Au₁₃₃ to a singly twinned Au₁₉₁

in the crossover size region and culminates with an untwinned fcc Au₂₇₉ nanomolecule.

Au₁₃₃ has an icosahedral core–shell structure with a 55-atom inner core and a 52-Au-atom surface anchoring pad to form the 107-atom metal core, Au@Au₁₂@Au₄₂@Au₅₂, protected by 26 monomeric staples with 26 Au atoms and 52 TBBT ligands.³¹ The Au₁₉₁ nanomolecule has a core–shell structure with 155 atoms, arranged as Au₃@Au₂₃@Au₆₃@Au₆₆, protected by 24 monomeric and 6 dimeric staples with 36 Au atoms and 66 TBBT ligands. Finally, Au₂₇₉ has a 147-atom cuboctahedral inner core with a 102-atom surface anchoring pad, to form the TO+ 249-atom core, Au@Au₁₂@Au₄₂@Au₉₂@Au₁₀₂, protected by 30 bridging ligands, 18 monomeric and 6 dimeric staples with 30 Au atoms and 84 TBBT ligands.³² The center to surface anchoring pad structure is a three-shell structure in Au₁₃₃ and Au₁₉₁, and a four-shell structure in Au₂₇₉ (see insets in Figure 5D). The core–shell structure of the inner core in Au₁₃₃ and Au₂₇₉ follows the mathematical formula for the magic number of shells in polyhedral clusters.⁸⁰

The structural evolution in the TBBT series crossover region and layer-wise bond-length analyses from the center to the surface anchoring pads and the center to the staple motifs are shown in Figures 5 and S8, respectively. Table S2 lists the bond-length analysis for Au₁₉₁ (average, standard deviation, and range); see ref 32 for the bond length analyses table on the Au₁₃₃ and Au₂₇₉ nanomolecules. The average interatomic distance of the D_{3h} -Au₈₉ inner core is 2.87 Å. It is close to the bulk Au–Au distance of 2.88 Å and similar to the untwinned Au₁₄₇ inner core of Au₂₇₉, whereas the multiply twinned I_h Au₅₅ inner core of the Au₁₃₃ has a slightly longer average distance of

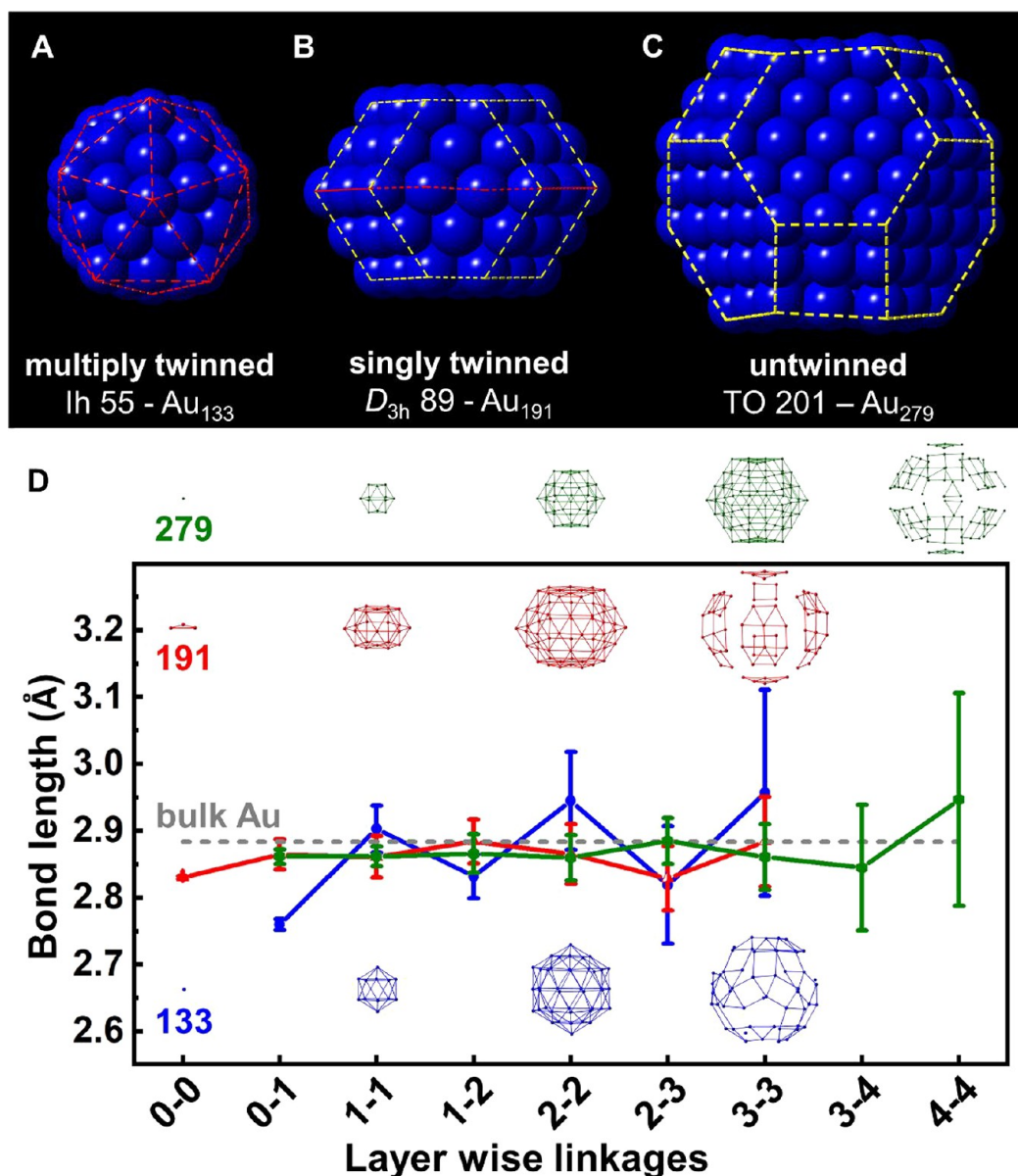


Figure 5. Structural evolution in the crossover region. (A) Multiply twinned icosahedral (I_h) 55-atom core in Au_{133} . (B) Monotwinned fcc D_{3h} 89-atom inner core in Au_{191} . (C) The untwinned bulk-like fcc truncated octahedral (TO) 201-atom core in Au_{279} . Color assignments in (A)–(C): twin boundaries, red dashed lines (A); untwinned facet boundaries, yellow dashed lines (B,C); blue, Au atoms (A–C). (D) Bond length analyses of the Au core from the center to the surface. X-axis: 0–0, center to center; 0–1, center to shell 1; 1–1, shell 1 to shell 1; ...4–4, shell 4 to shell 4. The plot includes the average bond length with standard deviation, and the inset displays the shell-wise images for each size. Blue ●, Au_{107} core in Au_{133} ; red ▲, Au_{155} core in Au_{191} ; olive ●, Au_{249} core in Au_{279} ; gray dashed line, bulk Au–Au bond distance. Table S2 lists the bond length analysis.

2.89 Å. The average bond length from the center to the surface ranges from 2.76 to 2.96 Å, 2.83 to 2.88 Å, and 2.86 to 2.95 Å in Au_{133} , Au_{191} , and Au_{279} , respectively (Figure 5D).

The distance of the surface anchoring pads from the inner core is ordered as Au_{133} (2.82 Å) < Au_{191} (2.83 Å) < Au_{279} (2.84 Å). The interatomic distance in the surface anchoring pads appears in the order Au_{191} (2.88 Å) < Au_{279} (2.93 Å) < Au_{133} (2.96 Å). Also, there is little or no hint of any strain at this interface, unlike the case in Au_{279} and Au_{133} .^{7,31,32} The distance of the staple Au sites from the anchoring pads is ordered as Au_{133} (3.19 Å) > Au_{191} (3.05 Å) > Au_{279} (2.99 Å). The average Au–S bond length does not vary much in all three structures, and the bond length ranges from 2.21 to 2.45 Å. Of note, pioneering work on Pd and Ag metal nanoparticles has

revealed multiply twinned I_h core structures similar to those found in the AuNMs.^{81–84}

Mass Spectrometry. Electrospray ionization mass spectrometry (ESI–MS) data reveal the 2+, 3+, and 4+ charge states (m/z , mass/charge) of Au_{191} (TBBT)₆₆ at 24 264, 16 176, and 12 132 Da, respectively (Figure 6A). The molecular weight of the compound was found to be 48 528 Da by deconvoluting the multiple charge state peaks, and the composition was assigned as Au_{191} (TBBT)₆₆. Also, Au_{191} (TBBT)₆₆ has a preferred charge state of 1+ (Figure S10). Matrix-assisted laser desorption ionization (MALDI) MS was carried out under threshold and high laser fluence to assess the purity and composition (Figure 6B). The threshold laser fluence data (red trace) reveal 1+ and 2+ peaks at ~46.1 and ~23.1 kDa, respectively (observed m/z is less than ~48.5 kDa

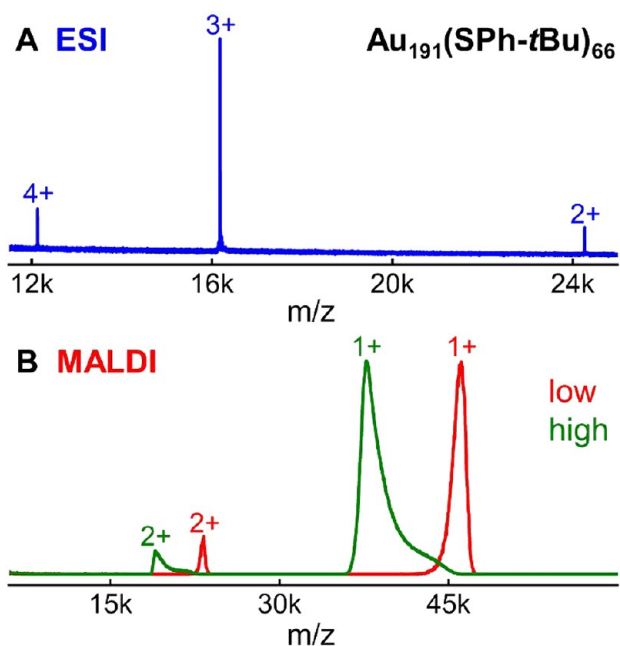


Figure 6. Mass spectrometry of the $\text{Au}_{191}(\text{SPh-tBu})_{66}$ nanomolecules. (A) ESI-MS data. (B) MALDI-MS, threshold low (red) and high (olive) laser fluence data.

due to fragmentation). The high laser data reveal the 1+ and 2+ peaks of the core at ~ 37.7 and ~ 18.9 kDa, respectively. The purity of the sample can be seen readily by the absence of any other peaks.

Steady-State Optical Absorption Properties. The absorption spectra and photon energy plot for the TBBT-capped Au_{191} in comparison with Au_{133} and Au_{279} reveal the transition from molecular to metallic behavior (Figure 7A,B). The Au_{191} record shows discrete features at 450 and 520 nm. The broad shoulder at 520 nm is reminiscent of an emergent surface plasmon resonance (SPR). The Au_{133} nanomolecule exhibits absorption features at 430, 510, and 700 nm, and the Au_{279} nanocrystal exhibits metal-like SPR at 510 nm. TDDFT simulated spectra predict its overall appearance with a small red-shift and accurately reproduce the overall trend with size (Figures 7 and S12). The influence of the Au_{191} anisotropic geometry is reflected in the different Cartesian components of the simulated spectrum; the Y component exhibits a more pronounced incipiently plasmonic peak at ~ 550 nm (Figure 7C). Independent component maps of oscillator strength (ICM-OS) plots for the most plasmonic, Y-Cartesian component were studied at 2.02 and 2.62 eV (Figure S13). It confirms some incipient, but not fully developed, preplasmonic features, with low intensity at 2.02 eV and restricted to a limited region of the occupied/virtual space.

Janus Molecular and Metallic Nature Revealed by Transient Absorption Studies. Molecular and metal-like excitation dynamics of AuNMs may be best revealed with the use of ultrafast transient absorption (TA) measurements.^{35,85,86} Molecule-like single particle excitations show broad positive excited-state absorption (ESA) and pump-power independent kinetics, whereas strong plasmonic bleach and pump-power dependent kinetics are the hallmarks of electron dynamics in metallic AuNMs.³⁵ To unravel the molecule/metallic nature of AuNMs, ultrafast TA measurements were carried out after excitation at 370 nm. The TA surface and spectra are shown in Figures 7 and S14–S16.

The Au_{191} transient data show a negative bleach with a maximum at ~ 540 nm, and a positive ESA on either side of the bleach, which grows with time until a time delay of 820 fs (Figures 7 and S15). Such growth is typical of metallic AuNPs and signifies the electron–electron thermalization processes. With time, the bleach is recovered to give rise to a broad, featureless, ESA at longer time delays. The bleach recovery is assigned to electron–phonon (e–p) relaxation. These spectral features are characteristic of metallic AuNPs with the bleach arising from plasmonic absorption. The recorded TA map for the Au_{191} nanomolecule in comparison with those for Au_{133} and Au_{279} is shown in Figure 7D–F. At 0.5 ps time delay, the Au_{133} displays two positive ESA features at 580 and 650 nm and a small bleach at ~ 510 nm, while the Au_{191} and Au_{279} nanomolecules exhibit plasmon bleach at ~ 540 nm (Figure 7G).

Species Associated Spectra. Three main components were observed in the Au_{191} relaxation dynamics species associated spectra. Au_{191} has a 2 ps bleach recovery component for e–p relaxation, followed by an 18 ps component and a long-lived species (Figure 7H); the 18 ps component has two bleach maxima at 510 and 560 nm. The e–p relaxation component (2 ps) is significantly longer than that of Au_{279} (1 ps) and the larger metallic AuNPs,^{59,85} but comparable to that of $\text{Au}_{329}(\text{SC}_2\text{H}_4\text{Ph})_{84}$ (1.4 ps).⁸⁵ The unique 18 ps and long-lived species were not observed in other small-sized plasmonic AuNPs. The emergence of these spectral features shows that the Au_{191} nanomolecule possesses excitonic states characteristic to particles of molecule-like nature.

Pump-Power Dependence. TA measurements at different pump fluence were carried out to explore the power-dependent kinetics (Figures 7I and S16). The Au_{191} spectral features were similar at all pump fluences, and three components were able to describe the relaxation dynamics (Figure S16). Interestingly, the contribution of all three components increased with an increase in pump fluence. The e–p relaxation time increased with an increase in the pump-power (Figure 7I,J), and it can be described accurately using a two-temperature model.⁴⁰ The strong power dependence of the e–p relaxation confirms the metal-like character of the Au_{191} nanomolecule. It is interesting to note that the slope of the e–p relaxation versus pump fluence is similar for Au_{191} and Au_{279} but is greatly different from that of Au_{133} (that shows molecule-like exciton dynamics and pump-power independent kinetics); see Figures 7J and S14. In contrast, the intrinsic e–p relaxation time is significantly (~ 2 -fold) longer for Au_{191} (1.8 ± 0.1 ps) when compared to Au_{279} (1.0 ± 0.1 ps).⁵⁹ The electron dynamics in transition from molecule to metal is schematically illustrated in Figure S17.

The experimental and computational results also indicate that the ligand conjugation and coupling among excitations associated with the metal core, the Au–S shell, and the aromatic residues are key in anticipating the birth of a plasmonic-like response, and to confer upon the Au_{191} nanomolecule its unique characteristics. The important contribution of organic residues to these quantities is apparent in the decomposition of the optical response into atomic components as displayed in Figure S18, and it can be further clearly appreciated from the plots of the induced density (Figure 7K) and induced electrostatic potential (Figure 7L) calculated via TDDFT/VS98 for the main peak at 2.21 eV. The induced, or transition, density is defined in eq S4.5 of ref 87; its plot displays the changes in electron density (with a

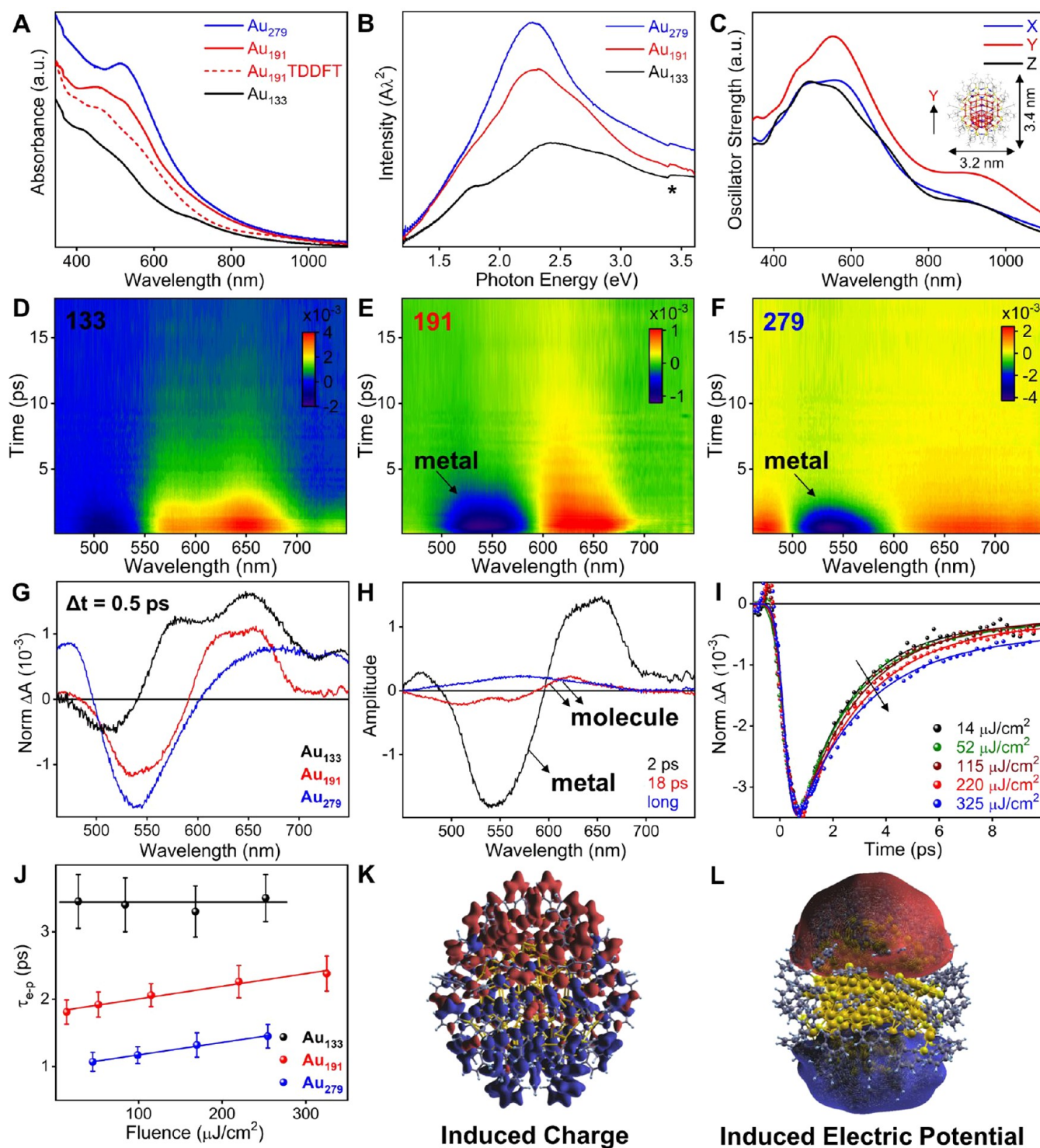


Figure 7. Optical properties displaying the Janus (molecular and metallic) nature of the Au₁₉₁ nanomolecule. (A) Steady-state absorption spectra of the Au₁₃₃, Au₁₉₁, and Au₂₇₉ (experiment) and Au₁₉₁ (simulated) nanomolecules. (B) Photon energy plot of the Au₁₃₃, Au₁₉₁, and Au₂₇₉ (experiment, *instrumental artifact) nanomolecules. (C) TDDFT optical absorption of Au₁₉₁ distinguished into Cartesian components. Figure S11 and the inset show the Cartesian axes orientation. Measured transient absorption, TA, surfaces are shown in (D) Au₁₃₃, (E) Au₁₉₁, and (F) Au₂₇₉ from 0.1 to 18 ps at 115 $\mu\text{J}/\text{cm}^2$ fluence. (G) TA spectra of Au₁₃₃, Au₁₉₁, and Au₂₇₉ at 0.5 ps time delay. (H) Species-associated spectra of Au₁₉₁ (from global fit analysis). (I) Principal kinetic decay traces obtained from single value decomposition analysis of Au₁₉₁ for different pump fluence (solid, multiexponential fitted traces). (J) Electron–phonon (e–p) relaxation time versus fluence. (K) Induced charge and (L) induced electric potential simulated via TDDFT/VS98 for the excitation at 2.21 eV.

positive or negative sign) induced by the exciting field, which thus provides a visual representation of an excitation at the given energy,⁸⁸ whereas the induced electrostatic potential is

the corresponding response Coulomb potential generated by the induced density. It is pertinent to comment here that in investigations of AuNMs, the ligands dictate the composition,

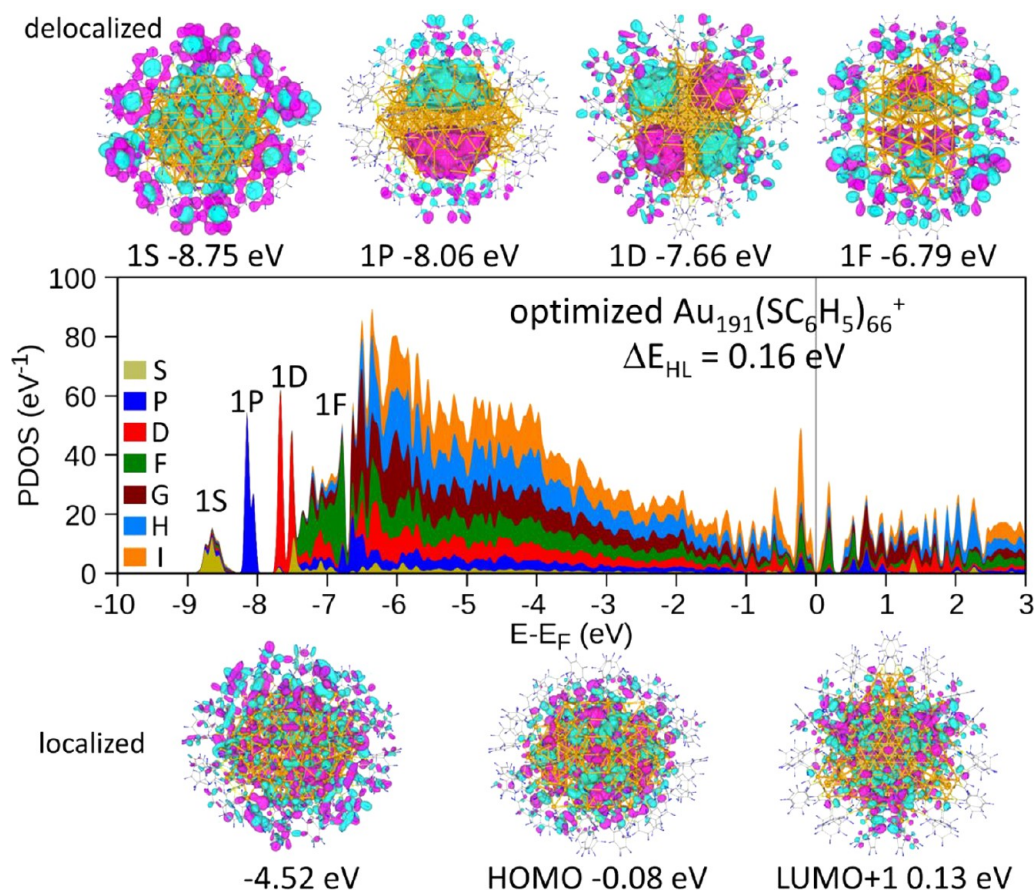


Figure 8. Electronic structure of the $\text{Au}_{191}(\text{SPh})_{66}$ nanomolecule. Calculated angular momentum projected densities of states (PDOS) for the $\text{Au}_{191}(\text{S-phenyl})_{66}$ nanomolecule. Displayed above and below are iso-surfaces of orbitals of selected electronic states of the ligand-capped cluster, superimposed on the optimized X-ray determined atomic configuration. Different colors (magenta and purple) correspond to opposite signs of the wave function, separated by nodal planes. The 1S, 1P, 1D, and 1F orbitals shown at the top (all corresponding to states at the bottom part of the PDOS spectrum) display delocalized, superatom, characteristics. The orbitals shown at the bottom, corresponding to the marked energies, are of localized nature, and any symmetry that they display reflects that of the atomic arrangements, the structural symmetry (note in particular the ones near the Fermi level). The various angular momenta contributions to the PDOS are displayed in different colors, as given in the inset.

structure, and properties, to form a unique discrete series of sizes based on the type of ligand.⁷ The optical properties have been widely studied in the aliphatic and aromatic thiolate protected series of AuNMs.^{35,59} Additionally, sometimes various sizes from different series have been considered as one AuNMs system.⁸⁶ It is better to compare each series separately, especially in the crossover region, as it provides a clear understanding and the contribution from the ligands to the optoelectronic property and control over the structure is common to all of the nanomolecules being studied and compared. It is to be noted that, although $\text{Au}_{191}(\text{TBBT})_{66}$ is smaller in size as compared to $\text{Au}_{246}(\text{p-MBT})_{80}$ (refs 34 and 86), the difference in capping ligands and atomic structure influences the properties of the nanomolecules. Therefore, in the *para*-methylbenzene thiolate (*p*-MBT) series, the molecular nature of the properties of the $\text{Au}_{246}(\text{p-MBT})_{80}$ nanomolecule being not bulk-like indicates that the crossover region to bulk-metal-like behavior for that series requires further investigation.^{34,86}

Electronic Structure of the Thiolate-Capped Au_{191} Nanomolecule and Electronic and Geometric Stabilization of the $D_{3h}\text{-Au}_{89}$ Inner Core. Insights pertaining to the electronic structure and stability of the thiolate-ligand-capped Au_{191} nanomolecule have been gained through calculations using the density-functional theory (DFT) method, which

employs the Vienna ab initio simulation package VASP;^{89–93} for further details, see the method section in the [Supporting Information](#). Results obtained with the use of these theoretical simulations subsequent to optimization of the thiolate-capped nanomolecule structure (starting from the X-ray crystal structure) are given in [Figures 8 and 9](#).

The projected density of states, PDOS, that is, the electronic density of states projected onto the angular momentum components,⁹⁴ calculated for the $\text{Au}_{191}(\text{SR})_{66}$ nanomolecule, is displayed in [Figure 8](#). In the calculations of the PDOS, the TBBT capping ligand is modeled (for computational convenience) by thiol-phenyl, that is, SR = S-phenyl; we have shown previously⁵⁴ that for larger capped Au_n clusters ($n > 100$), the PDOS results are relatively insensitive to such replacement.

The PDOS spectrum of the energy-optimized X-ray structure shows a rather small gap (referred to as the HOMO-LUMO gap, $\Delta E_{\text{HL}} = 0.16$ eV) between the highest occupied molecular orbital (HOMO) and the lowest unoccupied MO (LUMO) manifolds; see [Figure 8](#) in the region near the vertical dashed line at $E - E_{\text{F}} = 0$, where E_{F} is the Fermi level. Furthermore, inspection of the electronic structure shows clear evidence for delocalized states at the bottom part of the spectrum [see iso-surfaces of selected electronic orbitals that are classified according to their angular

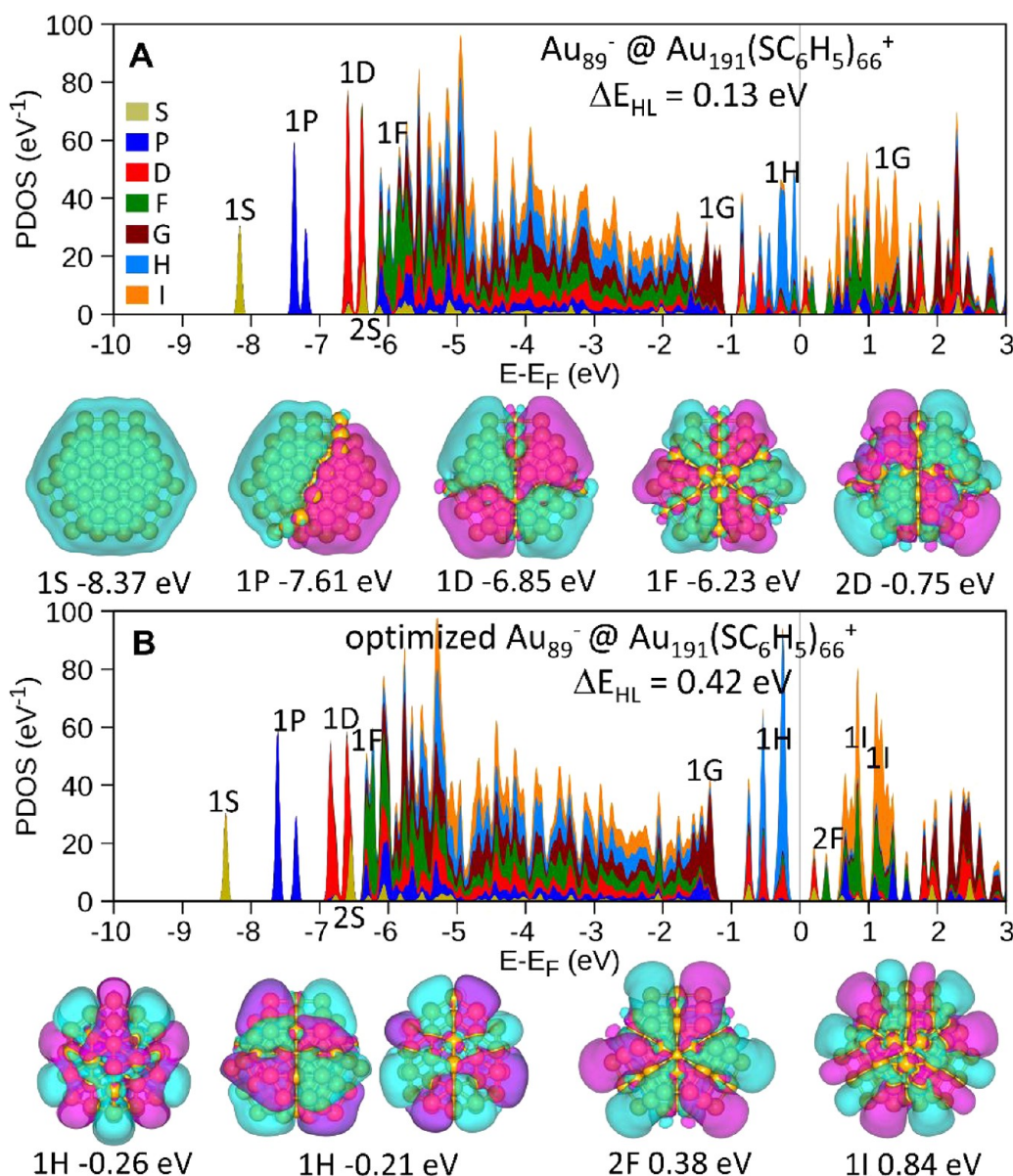


Figure 9. Electronic and structural stabilities of the nanoparticle inner core. Calculated angular momentum PDOS for (A) the Au_{89}^- inner core in the geometry it is found in the capped 191-gold-atom cluster, denoted as $\text{Au}_{89}^- @ \text{Au}_{191}(\text{S-phenyl})_{66}^+$ and for (B) the structurally relaxed $\text{Au}_{89}^- @ \text{Au}_{191}(\text{S-phenyl})_{66}^+$ inner core. Note the opening of the gap, $\Delta E_{\text{HL}} = 0.42$ eV. Also shown in (B) are iso-surfaces of superatom orbitals of the relaxed core. Different colors (magenta and purple) correspond to opposite signs of the wave function, separated by nodal planes. The various angular momenta contributions to the PDOS are displayed in different colors, as given in the inset to panel (A).

momenta, marked as $L = 1\text{S}, 1\text{P}, 1\text{D},$ and 1F , Figure 8, top]; these (superatom) states get occupied by the $6s^1$ electrons of the Au atoms. On the other hand, for the rest of the spectrum (e.g., in the middle and near the top of the occupied part of the spectrum, near $E - E_{\text{F}} = 0$), the electronic wave functions exhibit (see bottom of Figure 8) localized, molecule-like nature (associated with Au atomic 5d electrons), and any symmetric patterns displayed by these orbitals reflect structural (atomic arrangement) symmetries, rather than angular momentum symmetries (like the ones discussed above, shown at the top of Figure 8). We note here first that the above-noted behavior of the electronic structure of the cluster and the orbitals' angular momentum symmetries at the bottom part of the spectrum (Figure 8) agrees, in general, with an early proposal (introduced in ref 94) termed as a "partial jellium" model;

this methodology has been subsequently used in a number of investigations of ligand-capped metal clusters.^{21,95}

The above-noted superatom picture is tantamount to the well-known cluster-shell model⁶⁴ (CSM), which itself is an adaptation of the original nuclear-shell model. Accordingly, a CSM, or superatom, aufbau scheme is adopted, where the electron filling follows the following rule: $1\text{S}^2|1\text{P}^6|1\text{D}^{10}|2\text{S}^2|1\text{F}^{14}|2\text{P}^6|1\text{G}^{18}|2\text{D}^{10}|1\text{H}^{22}|3\text{S}^2|1\text{I}^{26} \dots$. The shell-closures (magic numbers) are denoted by vertical lines, and a closure near E_{F} is often accompanied by the opening of a stabilizing energy gap (referred to as the HOMO-LUMO gap, ΔE_{HL}). The "magic numbers", that is, the number of electrons completing the shells, take the following values: $n^* = 2, 8, 18, 20, 34, 40, 58, 90, 92, \dots$ electrons. The above aufbau rule and magic number sequence result from the assumed spherical (or near-spherical) cluster shape. Deviations of the cluster geometry from the

assumed spherical shape bring about lifting of the $g = 2L + 1$ degeneracy of the levels belonging to the L th angular momentum shell (see, for example, the split 1S, 1P, 1D, and 1F states in Figure 8). In condensed matter and molecule physics, such degeneracy-lifting is commonly termed as crystal-field level-splitting (for further discussion of shape effects on cluster electronic spectra, see refs 96 and 97).

The hallmarks of electronic stabilization in nanoparticles are the emergence of a gap between the HOMO and LUMO manifolds and of superatom shell-closure near the Fermi level. With both of the above attributes unobserved in the PDOS spectrum of the capped AuNPs (Figure 8), we turn next, in an attempt to unravel the spectral behavior near the Fermi level, to an analysis that focuses on the inner core of the NP, the Au₈₉ inner core cluster that is not bonded to ligands. The PDOS for that core in an anion charge state shows a similarly small gap $\Delta E_{\text{HL}} = 0.13$ eV, but a significantly changed energy level structure near $E - E_{\text{F}} = 0$ (Figure 9A). In fact, at the top of the occupied manifold, we observe the development of superatom shell structure with occupied 1G, 2D, and 1H levels. These levels that would be $(2L + 1)$ -fold degenerate for a spherically symmetric electronic confinement “crystal-field” split, as noted above, due to the nonspherical environment in which the 89-atom unit has been embedded, as well as that of the monotwinned stacking-faulted fcc Wulff underlying polyhedral inner core Au₈₉ cluster (see Figures 1, 4, S, and S4).

Structural relaxation of the Au₈₉⁻@Au₁₉₁(SPh)₆₆ core yields a PDOS of a significantly higher-level degeneracy with the development of superatom orbitals portraying a clear delocalized character, which extends from the occupied HOMO region to the unoccupied LUMO manifold (see Figure 9B). As aforementioned, the remaining observed splitting of the 1G, 2D, 1H, 2F, and 1I superatom orbitals in the HOMO and LUMO regions results from the nonspherical geometry of the relaxed crystalline Au₈₉ inner core. Together with the superatom shell structure at the bottom of the nanoparticle, the shell structure scheme of the Au₈₉⁻@Au₁₉₁(SPh)₆₆ core unit is $\{1S^2|1P^6|1D^{10}|2S^2|1F^{14}|2P^6|1G^{18}|2D^{10}|1H^{22}\}[3S^2|2I^{26}\dots]$, with $\{\dots\}$ denoting the occupied superatom levels (holding a total of $n^* = 90$ electron) and $[\dots]$ the unoccupied ones. This development is accompanied by the emergence of a significant gap $\Delta E_{\text{HL}} = 0.42$ eV, which attests to the electronic shell-structure stabilization of the inner core unit. This analysis leads us to conclude that the stability of the Au₁₉₁(SR)₆₆ nanoparticle originated from combined electronic stabilization (operative through the formation of a superatom shell structure of the 89-atom core) and geometrical (atomic structure) stabilization of the surrounding outer atomic shells and capping ligands.

Recently, we have termed the above analysis as the “core-cluster shell-model” (CCSM)⁵⁴ with the stabilization (associated with the opening of a relatively large ΔE_{HL} gap) resulting from organization of the superatom (shell) energy levels originating from electrons of the metal atoms residing in the core region of the ligand-capped nanoparticle [here the Au 6s¹ electrons of the Au₈₉⁻@Au₁₉₁(SPh)₆₆ inner core cluster]. This CCSM replaces here the commonly employed prescription for using the superatom shell-model of thiolate-capped $M_{N_A}(\text{SR})_m$ (e.g., M = Ag, Au) clusters^{21,95} (which itself generalized the bare-cluster partial-jellium model¹⁹⁴), where the number of valence electrons contributing to the superatom level structure is taken as $N_v = N_A - m$, i.e. the difference

between the total number of metal atoms (N_A) in the nanoparticle and the number of capping ligands (m). For example, for the present case of the Au₁₉₁(TBBT)₆₆ cluster, the conventional prescription would yield $N_v = 191 - 66 = 125$ electrons. On the other hand, in the CCSM, the superatom stabilization derives only from the inner core (IC) metal atoms, $N_{\text{A,IC}} < N_A$ (nonbonded directly to the sulfur atoms); for the Au₁₉₁(TBBT)₆₆ cluster considered here, this inner core consists of the singly twinned Au₈₉⁻ inner core cluster (with $N_v = N_{\text{A,IC}} + 1 = 90$).

As shown elsewhere,⁵⁴ as well as illustrated by us here, the CCSM methodology is most useful for cases where only a small, or no, ΔE_{HL} gap and no delocalized superatom orbitals near the Fermi level are found in the density of states of the entire capped nanoparticle. Focusing in the CCSM model on the electronic structure of the inner core region is further motivated by considering the cluster-growth process. Indeed, we expect that the electronic and geometric stability of the earlier-formed nucleating inner core of the metal nanoparticle (made of atoms that do not directly contact the capping organic ligand), and in particular the stabilization of that inner core due to its emergent superatom shell structure, would be transferred to the (subsequently assembling) outer atomic shells comprised of metal atoms that do interact and anchor (bind) the capping organic ligands.

To summarize, examination of the electronic structure following the CCSM methodology led to the discovery of the above-noted Au₈₉ cluster, predicted here to impart electronic stability (opening a shell-closing gap around the Fermi level) and the emergence of a compact stable structural motif, which we term as monotwinned/stacking-faulted Wulff face-centered-cubic polyhedron, or in short mt/sf-fcc nanocluster. Previous mention of monotwinning, and/or stacking-faults and glide/slip planes, in fcc nanoparticles as a stable structural motif may be found in some early literature on the properties of metal clusters,⁶⁸ gold nanomolecules,³ and other crystalline gold nanostructures (in particular, gold nanowires^{98–100}), as well as in a more recent work on twinned fcc clusters.⁷⁰

CONCLUSIONS

The discovery of Au₁₉₁(SPh-*t*Bu)₆₆ reveals key details pertaining to the structure and property variations associated with the size-evolution of metal nanoparticles, particularly in the transition regime from molecule-like to bulk-metal-like behavior. Au₁₉₁ has an anisotropic monotwinned structure, with an Au₁₅₅ core protected by a ligand shell made of 24 monomeric and 6 dimeric staples. The Au₁₅₅ core is a “perfectly twinned” structure, whereas multiply twinned structures (such as in the Au₁₃₃ nanoparticle) do exhibit a solid angle deficiency, which results in residual strain. The inner core of the Au₁₉₁ nanoparticle is composed of an 89-atom inner core and 66 surface atoms as concentric shells of atoms with the count of Au₃@Au₂₃@Au₆₃@Au₆₆. The Au₁₅₅ core has D_{3h} symmetry, and the thiolate monolayer breaks the symmetry to a chiral D_3 symmetry. The Au₈₉ inner core as a convex polyhedra has its parentage as an fcc twin of the TO-116 polyhedron and adds a new morphological motif to the library of polyhedral structures. This structure also sheds light on the structural evolution in metal nanoparticles with sizes ranging from extreme multiple-twinning to bulk monocrystalline cores with no twinning. In this way, the monotwinned Au₁₉₁ nanomolecule provides the missing link between

molecular multiple-twinning and bulk-like untwinned fcc crystalline structure.

The Janus nature of the ligand-capped Au₁₉₁ nanomolecule is exhibited in its optical and electronic properties. The steady-state absorption spectrum reveals two distinct features at 450 and 520 nm with emergent plasmonic-like response, while its neighboring sizes in the TBBT series portray molecular-like (Au₁₃₃) and metallic-like (Au₂₇₉) characteristics. Transient absorption studies revealed that it exhibits both metal-like electron–phonon relaxation dynamics and molecule-like long-lived excited states. Au₁₉₁ occupies a unique transition region exhibiting hybrid molecule-like and metal-like properties. The nature of the electronic spectrum in the core and surface regions of this nanomolecule and the interactions between the core-gold and surface-gold atoms (with the ligands providing extended conjugation) underlie the observed plasmonic behavior. At the same time, this nanomolecule is small enough to sustain molecule-like spectral characteristics. Note that the electronic conjugation between metal-core/staples and aromatic ligands is indispensable to anticipate the insurgence of plasmonic effects at such small sizes as Au₂₇₉, as demonstrated in ref 59, or here for Au₁₉₁. Moreover, Au₁₉₁ is unique in its anisotropic structural arrangement, which is apparent in some nonmonotonic features of the bond distance analysis in the series (Figure 5D) and is clearly reflected in the anisotropy of the simulated absorption spectra along different Cartesian axes (see Figure 7C,K,L). We conclude that the above-noted hybrid, Janus, nature of the Au₁₉₁(SPh-*t*Bu)₆₆ nanomolecule derives from a combination of various aspects, including anisotropic atomic structure, symmetry,³⁷ electronic structure, the interactions between core-gold and surface-gold, and extended conjugation in the ligand shell.

The theoretically calculated angular-momentum projected density of states of the ligand-capped Au₁₉₁ nanoparticle shows both delocalized (superatom, Au 6s¹ in origin) and localized (Au 5d¹⁰ in origin) electron orbitals. The delocalized orbitals organize into a superatom spectrum that follows the widely used electronic shell-model of clusters.⁶⁴ In the core-cluster-shell-model (CCSM) analysis⁵⁴ of the Au₈₉ inner core, the proximity to the 92 (90) electron shell closings of the D_{3h}⁻ Au₈₉^(3- or 1-) (with the superscripts indicating the formal charge-states of the nanocrystallite) confers superatom magic number stability to the 89-gold-atom inner core, and to the entire capped missing-link Au₁₉₁ nanomolecule. Combined with the aforementioned atomic (structural, crystallographic) stability of the monotwinned stacking-faulted fcc nanoparticle, the electronic-shell closing noted here makes the inner core cluster “doubly magic”, thus conferring an extra degree of stability conducive to preserving its independent character, when the 66-Au-atom surface-layer is anchored to or templated on that 89-Au-atom inner core seed. We believe that the finding of this “missing-link” cluster in the evolutionary sequence of metal nanoparticles, all capped by the same ligand, and its unique Janus nature (revealed in its optical properties), will serve as a landmark and motivate further studies pertaining to basic research opportunities in the field of atomically precise finite-size materials’ systems and their potential utilization.

■ ASSOCIATED CONTENT

SI Supporting Information

The Supporting Information is available free of charge at <https://pubs.acs.org/doi/10.1021/jacs.0c05685>.

Experimental details, figures, and tables (PDF)

X-ray crystal structure data for 191_66 (C₆₆₀H₈₅₈Au₁₉₁S₆₆) (CCDC 2000392) (CIF)

■ AUTHOR INFORMATION

Corresponding Author

Amala Dass – Department of Chemistry and Biochemistry, University of Mississippi, Oxford, Mississippi 38677, United States; orcid.org/0000-0001-6942-5451; Email: amal@olemiss.edu

Authors

Naga Arjun Sakthivel – Department of Chemistry and Biochemistry, University of Mississippi, Oxford, Mississippi 38677, United States; orcid.org/0000-0001-8134-905X

Masoud Shabaninezhad – Department of Physics, Western Michigan University, Kalamazoo, Michigan 49008, United States; orcid.org/0000-0003-1435-8989

Luca Sementa – CNR-ICCOM & IPCF, Consiglio Nazionale delle Ricerche, Pisa I-56124, Italy

Bokwon Yoon – School of Physics, Georgia Institute of Technology, Atlanta, Georgia 30332, United States

Mauro Stener – Dipartimento di Scienze Chimiche e Farmaceutiche, Università di Trieste, Trieste I-34127, Italy; orcid.org/0000-0003-3700-7903

Robert L. Whetten – Department of Applied Physics and Materials Science, Northern Arizona University, Flagstaff, Arizona 86011, United States; orcid.org/0000-0002-9838-6823

Guda Ramakrishna – Department of Chemistry, Western Michigan University, Kalamazoo, Michigan 49008, United States; orcid.org/0000-0002-5288-8780

Alessandro Fortunelli – CNR-ICCOM & IPCF, Consiglio Nazionale delle Ricerche, Pisa I-56124, Italy; orcid.org/0000-0001-5337-4450

Uzi Landman – School of Physics, Georgia Institute of Technology, Atlanta, Georgia 30332, United States; orcid.org/0000-0002-1586-1554

Complete contact information is available at: <https://pubs.acs.org/doi/10.1021/jacs.0c05685>

Notes

The authors declare no competing financial interest.

■ ACKNOWLEDGMENTS

We gratefully acknowledge Dr. Allen G. Oliver, Ms. Charlotte Stern, Dr. Christos Malliakas, Dr. Pierre LeMagueres, and the 2019 American Crystallographic Association summer course for screening the crystals and their help with SC-XRD data analysis. We thank Dr. Fengrui Qu and Dr. Elizabeth Papish for the SC-XRD data collection. G.R. acknowledges the support of Western Michigan University-FRACAA and Dr. Gary Wiederrecht, Argonne National Laboratory, for help with the TA measurements. Use of the Center for Nanoscale Materials, an Office of Science user facility, was supported by the U.S. Department of Energy, Office of Science, Office of Basic Energy Sciences, under contract no. DE-AC02-06CH11357. NSF-CHE-1808138 and NSF-CHE-1255519 supported the work performed by N.A.S. and A.D. The work of B.Y. and U.L. has been supported by the Air Force Office of Scientific Research (AFOSR) under grant no. FA9550-15-1-0519. Calculations of the electronic structure were carried out

at the Georgia Institute of Technology Center for Computational Materials Science. We thank NSF-CHE-MRI-1828078 and the University of Alabama for the purchase of SC-XRD instrument. A.F., L.S., and M.S. acknowledge the support from the Cineca Supercomputing Center for TDDFT simulations and analysis.

REFERENCES

- (1) Faraday, M. The Bakerian Lecture. —Experimental relations of gold (and other metals) to light. *Philos. Trans. R. Soc. London* **1857**, *147*, 145–181.
- (2) Brust, M.; Walker, M.; Bethell, D.; Schiffrin, D. J.; Whyman, R. Synthesis of Thiol-Derivatized Gold Nanoparticles in a Two-Phase Liquid-Liquid System. *J. Chem. Soc., Chem. Commun.* **1994**, *0*, 801–802.
- (3) Whetten, R. L.; Khoury, J. T.; Alvarez, M. M.; Murthy, S.; Vezmar, I.; Wang, Z. L.; Stephens, P. W.; Cleveland, C. L.; Luedtke, W. D.; Landman, U. Nanocrystal Gold Molecules. *Adv. Mater.* **1996**, *8*, 428–433.
- (4) Hostetler, M. J.; Green, S. J.; Stokes, J. J.; Murray, R. W. Monolayers in Three Dimensions: Synthesis and Electrochemistry of ω -Functionalized Alkanethiolate-Stabilized Gold Cluster Compounds. *J. Am. Chem. Soc.* **1996**, *118*, 4212–4213.
- (5) Jadzinsky, P. D.; Calero, G.; Ackerson, C. J.; Bushnell, D. A.; Kornberg, R. D. Structure of a Thiol Monolayer-Protected Gold Nanoparticle at 1.1 Å Resolution. *Science* **2007**, *318*, 430–433.
- (6) Parker, J. F.; Fields-Zinna, C. A.; Murray, R. W. The Story of a Monodisperse Gold Nanoparticle: Au₂₅L₁₈. *Acc. Chem. Res.* **2010**, *43*, 1289–1296.
- (7) Sakthivel, N. A.; Dass, A. Aromatic Thiolate-Protected Series of Gold Nanomolecules and a Contrary Structural Trend in Size Evolution. *Acc. Chem. Res.* **2018**, *51*, 1774–1783.
- (8) Yang, H.; Wang, Y.; Chen, X.; Zhao, X.; Gu, L.; Huang, H.; Yan, J.; Xu, C.; Li, G.; Wu, J.; Edwards, A. J.; Dittrich, B.; Tang, Z.; Wang, D.; Lehtovaara, L.; Häkkinen, H.; Zheng, N. Plasmonic Twinned Silver Nanoparticles with Molecular Precision. *Nat. Commun.* **2016**, *7*, 12809.
- (9) Yan, J.; Teo, B. K.; Zheng, N. Surface Chemistry of Atomically Precise Coinage–Metal Nanoclusters: From Structural Control to Surface Reactivity and Catalysis. *Acc. Chem. Res.* **2018**, *51*, 3084–3093.
- (10) Hossain, S.; Niihori, Y.; Nair, L. V.; Kumar, B.; Kurashige, W.; Negishi, Y. Alloy Clusters: Precise Synthesis and Mixing Effects. *Acc. Chem. Res.* **2018**, *51*, 3114–3124.
- (11) Chakraborty, I.; Pradeep, T. Atomically Precise Clusters of Noble Metals: Emerging Link between Atoms and Nanoparticles. *Chem. Rev.* **2017**, *117*, 8208–8271.
- (12) Lei, Z.; Li, J.-J.; Wan, X.-K.; Zhang, W.-H.; Wang, Q.-M. Isolation and Total Structure Determination of an All-Alkynyl-Protected Gold Nanocluster Au₁₄₄. *Angew. Chem., Int. Ed.* **2018**, *57*, 8639–8643.
- (13) Yan, N.; Xia, N.; Liao, L.; Zhu, M.; Jin, F.; Jin, R.; Wu, Z. Unraveling the Long-Pursued Au₁₄₄ Structure by X-Ray Crystallography. *Sci. Adv.* **2018**, *4*, No. eaat7259.
- (14) Nieto-Ortega, B.; Bürgi, T. Vibrational Properties of Thiolate-Protected Gold Nanoclusters. *Acc. Chem. Res.* **2018**, *51*, 2811–2819.
- (15) Liu, J.-Y.; Alkan, F.; Wang, Z.; Zhang, Z.-Y.; Kurmoo, M.; Yan, Z.; Zhao, Q.-Q.; Aikens, C. M.; Tung, C.-H.; Sun, D. Different Silver Nanoparticles in One Crystal: Ag₂₁₀(iPrPhS)₇₁(Ph₃P)₅Cl and Ag₂₁₁(iPrPhS)₇₁(Ph₃P)₆Cl. *Angew. Chem., Int. Ed.* **2019**, *58*, 195–199.
- (16) Wong, O. A.; Hansen, R. J.; Ni, T. W.; Heinecke, C. L.; Compel, W. S.; Gustafson, D. L.; Ackerson, C. J. Structure-Activity Relationships for Biodistribution, Pharmacokinetics, and Excretion of Atomically Precise Nanoclusters in a Murine Model. *Nanoscale* **2013**, *5*, 10525–10533.
- (17) Yi, C.; Tofanelli, M. A.; Ackerson, C. J.; Knappenberger, K. L. Optical Properties and Electronic Energy Relaxation of Metallic Au₁₄₄(SR)₆₀ Nanoclusters. *J. Am. Chem. Soc.* **2013**, *135*, 18222–18228.
- (18) De Nardi, M.; Antonello, S.; Jiang, D.-e.; Pan, F.; Rissanen, K.; Ruzzi, M.; Venzo, A.; Zoleo, A.; Maran, F. Gold Nanowired: A Linear (Au₂₅)_n Polymer from Au₂₅ Molecular Clusters. *ACS Nano* **2014**, *8*, 8505–8512.
- (19) Alhilaly, M. J.; Huang, R.-W.; Naphade, R.; Alamer, B.; Hedhili, M. N.; Emwas, A.-H.; Maity, P.; Yin, J.; Shkurenko, A.; Mohammed, O. F.; Eddaoudi, M.; Bakr, O. M. Assembly of Atomically Precise Silver Nanoclusters into Nanocluster-Based Frameworks. *J. Am. Chem. Soc.* **2019**, *141*, 9585–9592.
- (20) Quinn, B. M.; Liljeroth, P.; Ruiz, V.; Laaksonen, T.; Kontturi, K. Electrochemical Resolution of 15 Oxidation States for Monolayer Protected Gold Nanoparticles. *J. Am. Chem. Soc.* **2003**, *125*, 6644–6645.
- (21) Desireddy, A.; Conn, B. E.; Guo, J.; Yoon, B.; Barnett, R. N.; Monahan, B. M.; Kirschbaum, K.; Griffith, W. P.; Whetten, R. L.; Landman, U.; Bigioni, T. P. Ultrastable Silver Nanoparticles. *Nature* **2013**, *501*, 399–402.
- (22) Yoon, B.; Luedtke, W. D.; Barnett, R. N.; Gao, J.; Desireddy, A.; Conn, B. E.; Bigioni, T.; Landman, U. Hydrogen-Bonded Structure and Mechanical Chiral Response of A Silver Nanoparticle Superlattice. *Nat. Mater.* **2014**, *13*, 807–811.
- (23) Abbas, M. A.; Kamat, P. V.; Bang, J. H. Thiolated Gold Nanoclusters for Light Energy Conversion. *ACS Energy Letters* **2018**, *3*, 840–854.
- (24) Stampelcoskie, K. G.; Kamat, P. V. Synergistic Effects in the Coupling of Plasmon Resonance of Metal Nanoparticles with Excited Gold Clusters. *J. Phys. Chem. Lett.* **2015**, *6*, 1870–1875.
- (25) Liu, H.; Hong, G.; Luo, Z.; Chen, J.; Chang, J.; Gong, M.; He, H.; Yang, J.; Yuan, X.; Li, L.; Mu, X.; Wang, J.; Mi, W.; Luo, J.; Xie, J.; Zhang, X.-D. Atomic-Precision Gold Clusters for NIR-II Imaging. *Adv. Mater.* **2019**, *31*, 1901015.
- (26) Du, Y.; Sheng, H.; Astruc, D.; Zhu, M. Atomically Precise Noble Metal Nanoclusters as Efficient Catalysts: A Bridge between Structure and Properties. *Chem. Rev.* **2020**, *120*, 526–622.
- (27) Link, S.; El-Sayed, M. A. Optical Properties and Ultrafast Dynamics of Metallic Nanocrystals. *Annu. Rev. Phys. Chem.* **2003**, *54*, 331–366.
- (28) Murray, R. W. Nanoelectrochemistry: Metal Nanoparticles, Nanoelectrodes, and Nanopores. *Chem. Rev.* **2008**, *108*, 2688–2720.
- (29) Laaksonen, T.; Ruiz, V.; Liljeroth, P.; Quinn, B. M. Quantised Charging of Monolayer-Protected Nanoparticles. *Chem. Soc. Rev.* **2008**, *37*, 1836–1846.
- (30) Negishi, Y.; Nakazaki, T.; Malola, S.; Takano, S.; Niihori, Y.; Kurashige, W.; Yamazoe, S.; Tsukuda, T.; Häkkinen, H. A Critical Size for Emergence of Nonbulk Electronic and Geometric Structures in Dodecanethiolate-Protected Au Clusters. *J. Am. Chem. Soc.* **2015**, *137*, 1206–1212.
- (31) Dass, A.; Theivendran, S.; Nimmala, P. R.; Kumara, C.; Jupally, V. R.; Fortunelli, A.; Sementa, L.; Barcaro, G.; Zuo, X.; Noll, B. C. Au₁₃₃(SPh-tBu)₅₂ Nanomolecules: X-ray Crystallography, Optical, Electrochemical, and Theoretical Analysis. *J. Am. Chem. Soc.* **2015**, *137*, 4610–4613.
- (32) Sakthivel, N. A.; Theivendran, S.; Ganeshraj, V.; Oliver, A. G.; Dass, A. Crystal Structure of Faradaurate-279: Au₂₇₉(SPh-tBu)₈₄ Plasmonic Nanocrystal Molecules. *J. Am. Chem. Soc.* **2017**, *139*, 15450–15459.
- (33) Dass, A.; Sakthivel, N. A.; Jupally, V. R.; Kumara, C.; Rambukwella, M. Plasmonic Nanomolecules: Electrochemical Resolution of 22 Electronic States in Au₃₂₉(SR)₈₄. *ACS Energy Letters* **2020**, *5*, 207–214.
- (34) Zeng, C.; Chen, Y.; Kirschbaum, K.; Lambright, K. J.; Jin, R. Emergence of Hierarchical Structural Complexities in Nanoparticles and their Assembly. *Science* **2016**, *354*, 1580–1584.
- (35) Kwak, K.; Thanthirige, V. D.; Pyo, K.; Lee, D.; Ramakrishna, G. Energy Gap Law for Exciton Dynamics in Gold Cluster Molecules. *J. Phys. Chem. Lett.* **2017**, *8*, 4898–4905.

- (36) Malola, S.; Lehtovaara, L.; Enkovaara, J.; Häkkinen, H. Birth of the Localized Surface Plasmon Resonance in Monolayer-Protected Gold Nanoclusters. *ACS Nano* **2013**, *7*, 10263–10270.
- (37) Malola, S.; Kaappa, S.; Häkkinen, H. Role of Nanocrystal Symmetry in the Crossover Region from Molecular to Metallic Gold Nanoparticles. *J. Phys. Chem. C* **2019**, *123*, 20655–20663.
- (38) Xu, W. W.; Zeng, X. C.; Gao, Y. Application of Electronic Counting Rules for Ligand-Protected Gold Nanoclusters. *Acc. Chem. Res.* **2018**, *51*, 2739–2747.
- (39) Negishi, Y.; Nobusada, K.; Tsukuda, T. Glutathione-Protected Gold Clusters Revisited: Bridging the Gap between Gold(I)-Thiolate Complexes and Thiolate-Protected Gold Nanocrystals. *J. Am. Chem. Soc.* **2005**, *127*, 5261–5270.
- (40) Hartland, G. V. Optical Studies of Dynamics in Noble Metal Nanostructures. *Chem. Rev.* **2011**, *111*, 3858–3887.
- (41) Kubo, R. Electronic Properties of Metallic Fine Particles. I. *J. Phys. Soc. Jpn.* **1962**, *17*, 975–986.
- (42) Kawabata, A.; Kubo, R. Electronic Properties of Fine Metallic Particles. II. Plasma Resonance Absorption. *J. Phys. Soc. Jpn.* **1966**, *21*, 1765–1772.
- (43) Morton, S. M.; Silverstein, D. W.; Jensen, L. Theoretical Studies of Plasmonics using Electronic Structure Methods. *Chem. Rev.* **2011**, *111*, 3962–3994.
- (44) Fernando, A.; Weerawardene, K. L. D. M.; Karimova, N. V.; Aikens, C. M. Quantum Mechanical Studies of Large Metal, Metal Oxide, and Metal Chalcogenide Nanoparticles and Clusters. *Chem. Rev.* **2015**, *115*, 6112–6216.
- (45) Jensen, K. M. Ø.; Juhas, P.; Tofanelli, M. A.; Heinecke, C. L.; Vaughan, G.; Ackerson, C. J.; Billinge, S. J. L. Polymorphism in Magic-Sized Au₁₄₄(SR)₆₀ Clusters. *Nat. Commun.* **2016**, *7*, 11859.
- (46) Yau, S. H.; Varnavski, O.; Goodson, T. An Ultrafast Look at Au Nanoclusters. *Acc. Chem. Res.* **2013**, *46*, 1506–1516.
- (47) Rambukwella, M.; Sakhivel, N. A.; Delcamp, J. H.; Sementa, L.; Fortunelli, A.; Dass, A. Ligand Structure Determines Nanoparticles' Atomic Structure, Metal-Ligand Interface and Properties. *Front. Chem.* **2018**, *6*, 330.
- (48) Kwak, K.; Lee, D. Electrochemistry of Atomically Precise Metal Nanoclusters. *Acc. Chem. Res.* **2019**, *52*, 12–22.
- (49) Yamazoe, S.; Koyasu, K.; Tsukuda, T. Non-scalable Oxidation Catalysis of Gold Clusters. *Acc. Chem. Res.* **2014**, *47*, 816–824.
- (50) Wiseman, M. R.; Marsh, P. A.; Bishop, P. T.; Brisdon, B. J.; Mahon, M. F. Homoleptic Gold Thiolate Catenanes. *J. Am. Chem. Soc.* **2000**, *122*, 12598–12599.
- (51) Zeng, C.; Liu, C.; Chen, Y.; Rosi, N. L.; Jin, R. Gold–Thiolate Ring as a Protecting Motif in the Au₂₀(SR)₁₆ Nanocluster and Implications. *J. Am. Chem. Soc.* **2014**, *136*, 11922–11925.
- (52) Zeng, C.; Chen, Y.; Iida, K.; Nobusada, K.; Kirschbaum, K.; Lambright, K. J.; Jin, R. Gold Quantum Boxes: On the Periodicities and the Quantum Confinement in the Au₂₈, Au₃₆, Au₄₄ and Au₅₂ Magic Series. *J. Am. Chem. Soc.* **2016**, *138*, 3950–3953.
- (53) Liao, L.; Chen, J.; Wang, C.; Zhuang, S.; Yan, N.; Yao, C.; Xia, N.; Li, L.; Bao, X.; Wu, Z. Transition-Sized Au₉₂ Nanoparticle Bridging Non-FCC-Structured Gold Nanoclusters and FCC-Structured Gold Nanocrystals. *Chem. Commun.* **2016**, *52*, 12036–12039.
- (54) Sakhivel, N. A.; Sementa, L.; Yoon, B.; Landman, U.; Fortunelli, A.; Dass, A. Isomeric Thiolate Monolayer Protected Au₉₂ and Au₁₀₂ Nanomolecules. *J. Phys. Chem. C* **2020**, *124*, 1655–1666.
- (55) Zeng, C.; Liu, C.; Chen, Y.; Rosi, N. L.; Jin, R. Atomic Structure of Self-Assembled Monolayer of Thiols on a Tetragonal Au₉₂ Nanocrystal. *J. Am. Chem. Soc.* **2016**, *138*, 8710–8713.
- (56) Zhuang, S.; Liao, L.; Yuan, J.; Wang, C.; Zhao, Y.; Xia, N.; Gan, Z.; Gu, W.; Li, J.; Deng, H.; Yang, J.; Wu, Z. Kernel Homology in Gold Nanoclusters. *Angew. Chem., Int. Ed.* **2018**, *57*, 15450–15454.
- (57) Zhuang, S.; Liao, L.; Zhao, Y.; Yuan, J.; Yao, C.; Liu, X.; Li, J.; Deng, H.; Yang, J.; Wu, Z. Is the Kernel–Staples Match a Key–Lock Match? *Chem. Sci.* **2018**, *9*, 2437–2442.
- (58) Liao, L.; Wang, C.; Zhuang, S.; Yan, N.; Zhao, Y.; Yang, Y.; Li, J.; Deng, H.; Wu, Z. An Unprecedented Kernel Growth Mode and Layer-Number-Odevity-Dependent Properties in Gold Nanoclusters. *Angew. Chem., Int. Ed.* **2020**, *59*, 731–734.
- (59) Sakhivel, N. A.; Stener, M.; Sementa, L.; Fortunelli, A.; Ramakrishna, G.; Dass, A. Au₂₇₉(SR)₈₄: The Smallest Gold Thiolate Nanocrystal That Is Metallic and the Birth of Plasmon. *J. Phys. Chem. Lett.* **2018**, *9*, 1295–1300.
- (60) Schaaff, T. G.; Shafiqullin, M. N.; Khoury, J. T.; Vezmar, I.; Whetten, R. L.; Cullen, W. G.; First, P. N.; Gutiérrez-Wing, C.; Ascensio, J.; Jose-Yacamán, M. J. Isolation of Smaller Nanocrystal Au Molecules: Robust Quantum Effects in Optical Spectra. *J. Phys. Chem. B* **1997**, *101*, 7885–7891.
- (61) Negishi, Y.; Sakamoto, C.; Ohyama, T.; Tsukuda, T. Synthesis and the Origin of the Stability of Thiolate-Protected Au₁₃₀ and Au₁₈₇ Clusters. *J. Phys. Chem. Lett.* **2012**, *3*, 1624–1628.
- (62) Tlahuice-Flores, A. New Insight into the Structure of Thiolated Gold Clusters: A Structural Prediction of the Au₁₈₇(SR)₆₈ Cluster. *Phys. Chem. Chem. Phys.* **2015**, *17*, 5551–5555.
- (63) Dass, A. Faradaurate Nanomolecules: A Superstable Plasmonic 76.3 kDa Cluster. *J. Am. Chem. Soc.* **2011**, *133*, 19259–19261.
- (64) Knight, W. D.; Clemenger, K.; de Heer, W. A.; Saunders, W. A.; Chou, M. Y.; Cohen, M. L. Electronic Shell Structure and Abundances of Sodium Clusters. *Phys. Rev. Lett.* **1984**, *52*, 2141–2143.
- (65) P. K. Doye, J.; J. Wales, D. Structural Consequences of the Range of the Interatomic Potential a Menagerie of Clusters. *J. Chem. Soc., Faraday Trans.* **1997**, *93*, 4233–4243.
- (66) Cheng, L.; Yang, J. Novel Lattice-Searching Method for Modeling the Optimal Strain-Free Close-Packed Isomers of Clusters. *J. Phys. Chem. A* **2007**, *111*, 2336–2342.
- (67) Fotin, A.; Cheng, Y.; Sliz, P.; Grigorieff, N.; Harrison, S. C.; Kirchhausen, T.; Walz, T. Molecular Model for a Complete Clathrin Lattice from Electron Cryomicroscopy. *Nature* **2004**, *432*, 573–579.
- (68) Cleveland, C. L.; Landman, U. The Energetics and Structure of Nickel Clusters: Size Dependence. *J. Chem. Phys.* **1991**, *94*, 7376–7396.
- (69) Wulff, G. XXV. Zur Frage der Geschwindigkeit des Wachstums und der Auflösung der Kristallflächen. *Z. Kristallogr. - Cryst. Mater.* **1901**, *34*, 449–530.
- (70) Vergara, S.; Lukes, D. A.; Martynowycz, M. W.; Santiago, U.; Plascencia-Villa, G.; Weiss, S. C.; de la Cruz, M. J.; Black, D. M.; Alvarez, M. M.; López-Lozano, X.; Barnes, C. O.; Lin, G.; Weissker, H.-C.; Whetten, R. L.; Gonen, T.; Yacamán, M. J.; Calero, G. MicroED Structure of Au₁₄₆(p-MBA)₅₇ at Subatomic Resolution Reveals a Twinned FCC Cluster. *J. Phys. Chem. Lett.* **2017**, *8*, 5523–5530.
- (71) Johnson, N. W. Convex Polyhedra with Regular Faces. *Can. J. Math.* **1966**, *18*, 169–200.
- (72) Marks, L. D. Surface Structure and Energetics of Multiply Twinned Particles. *Philos. Mag. A* **1984**, *49*, 81–93.
- (73) Baletto, F.; Ferrando, R.; Fortunelli, A.; Montalenti, F.; Mottet, C. Crossover Among Structural Motifs in Transition and Noble-Metal Clusters. *J. Chem. Phys.* **2002**, *116*, 3856–3863.
- (74) Baletto, F.; Ferrando, R. Structural Properties of Nanoclusters: Energetic, Thermodynamic, and Kinetic Effects. *Rev. Mod. Phys.* **2005**, *77*, 371–423.
- (75) Barnard, A. S.; Lin, X. M.; Curtiss, L. A. Equilibrium Morphology of Face-Centered Cubic Gold Nanoparticles > 3 nm and the Shape Changes Induced by Temperature. *J. Phys. Chem. B* **2005**, *109*, 24465–24472.
- (76) Patala, S.; Marks, L. D.; Olvera de la Cruz, M. Thermodynamic Analysis of Multiply Twinned Particles: Surface Stress Effects. *J. Phys. Chem. Lett.* **2013**, *4*, 3089–3094.
- (77) Ferrando, R. Structure and Properties of Nanoalloys. In *Frontiers of Nanoscience*; Ferrando, R., Ed.; Elsevier: New York, 2016; Vol. 10, p 337.
- (78) Häberlen, O. D.; Chung, S.-C.; Stener, M.; Rösch, N. From Clusters to Bulk: A Relativistic Density Functional Investigation on A Series of Gold Clusters Au_n, n = 6, ..., 147. *J. Chem. Phys.* **1997**, *106*, 5189–5201.

- (79) Raoult, B.; Farges, J.; De Feraudy, M. F.; Torchet, G. Comparison between Icosahedral, Decahedral and Crystalline Lennard-Jones Models Containing 500 to 6000 Atoms. *Philos. Mag. B* **1989**, *60*, 881–906.
- (80) Teo, B. K.; Sloane, N. J. A. Magic Numbers in Polyagonal and Polyhedral Clusters. *Inorg. Chem.* **1985**, *24*, 4545–4558.
- (81) Tran, N. T.; Powell, D. R.; Dahl, L. F. Nanosized Pd₁₄₅(CO)_x(PET₃)₃₀ Containing a Capped Three-Shell 145-Atom Metal-Core Geometry of Pseudo Icosahedral Symmetry. *Angew. Chem., Int. Ed.* **2000**, *39*, 4121–4125.
- (82) Mednikov, E. G.; Jewell, M. C.; Dahl, L. F. Nanosized (μ_{12} -Pt)Pd_{164-x}Pt_x(CO)₇₂(PPH₃)₂₀ ($x \approx 7$) Containing Pt-Centered Four-Shell 165-Atom Pd-Pt Core with Unprecedented Intershell Bridging Carbonyl Ligands: Comparative Analysis of Icosahedral Shell-Growth Patterns with Geometrically Related Pd₁₄₅(CO)_x(PET₃)₃₀ ($x \approx 60$) Containing Capped Three-Shell Pd₁₄₅ Core. *J. Am. Chem. Soc.* **2007**, *129*, 11619–11630.
- (83) Yan, J.; Malola, S.; Hu, C.; Peng, J.; Dittrich, B.; Teo, B. K.; Häkkinen, H.; Zheng, L.; Zheng, N. Co-Crystallization of Atomically Precise Metal Nanoparticles Driven by Magic Atomic and Electronic Shells. *Nat. Commun.* **2018**, *9*, 3357.
- (84) Erickson, J. D.; Mednikov, E. G.; Ivanov, S. A.; Dahl, L. F. Isolation and Structural Characterization of a Mackay 55-Metal-Atom Two-Shell Icosahedron of Pseudo- I_h Symmetry, Pd₃₅L₁₂(μ_3 -CO)₂₀ (L = PR₃, R = Isopropyl): Comparative Analysis with Interior Two-Shell Icosahedral Geometries in Capped Three-Shell Pd₁₄₅, Pt-Centered Four-Shell Pd–Pt M₁₆₅, and Four-Shell Au₁₃₃ Nanoclusters. *J. Am. Chem. Soc.* **2016**, *138*, 1502–1505.
- (85) Shabaninezhad, M.; Abuhagr, A.; Sakthivel, N. A.; Kumara, C.; Dass, A.; Kwak, K.; Pyo, K.; Lee, D.; Ramakrishna, G. Ultrafast Electron Dynamics in Thiolate-Protected Plasmonic Gold Clusters: Size and Ligand Effect. *J. Phys. Chem. C* **2019**, *123*, 13344–13353.
- (86) Zhou, M.; Higaki, T.; Li, Y.; Zeng, C.; Li, Q.; Sfeir, M. Y.; Jin, R. Three-Stage Evolution from Non-scalable to Scalable Optical Properties of Thiolate-Protected Gold Nanoclusters. *J. Am. Chem. Soc.* **2019**, *141*, 19754–19764.
- (87) McWeeny, R. *Methods of Molecular Quantum Mechanics*, 2nd ed.; Academic Press: London, 1989; p 573.
- (88) Chang, L.; Baseggio, O.; Sementa, L.; Cheng, D.; Fronzoni, G.; Toffoli, D.; Aprà, E.; Stener, M.; Fortunelli, A. Individual Component Map of Rotatory Strength and Rotatory Strength Density Plots As Analysis Tools of Circular Dichroism Spectra of Complex Systems. *J. Chem. Theory Comput.* **2018**, *14*, 3703–3714.
- (89) Kresse, G.; Hafner, J. Ab Initio Molecular Dynamics for Liquid Metals. *Phys. Rev. B: Condens. Matter Mater. Phys.* **1993**, *47*, 558–561.
- (90) Kresse, G.; Hafner, J. Ab Initio Molecular-Dynamics Simulation of The Liquid-Metal–Amorphous-Semiconductor Transition In Germanium. *Phys. Rev. B: Condens. Matter Mater. Phys.* **1994**, *49*, 14251–14269.
- (91) Kresse, G.; Furthmüller, J. Efficient Iterative Schemes for Ab Initio Total-Energy Calculations using A Plane-Wave Basis Set. *Phys. Rev. B: Condens. Matter Mater. Phys.* **1996**, *54*, 11169–11186.
- (92) Kresse, G.; Furthmüller, J. Efficiency of Ab-Initio Total Energy Calculations for Metals and Semiconductors using A Plane-Wave Basis Set. *Comput. Mater. Sci.* **1996**, *6*, 15–50.
- (93) Kresse, G.; Joubert, D. From Ultrasoft Pseudopotentials to The Projector Augmented-Wave Method. *Phys. Rev. B: Condens. Matter Mater. Phys.* **1999**, *59*, 1758–1775.
- (94) Yoon, B.; Koskinen, P.; Huber, B.; Kostko, O.; von Issendorff, B.; Häkkinen, H.; Moseler, M.; Landman, U. Size-Dependent Structural Evolution and Chemical Reactivity of Gold Clusters. *ChemPhysChem* **2007**, *8*, 157–161.
- (95) Walter, M.; Akola, J.; Lopez-Acevedo, O.; Jadzinsky, P. D.; Calero, G.; Ackerson, C. J.; Whetten, R. L.; Grönbeck, H.; Häkkinen, H. A Unified View of Ligand-Protected Gold Clusters as Superatom Complexes. *Proc. Natl. Acad. Sci. U. S. A.* **2008**, *105*, 9157–9162.
- (96) Yannouleas, C.; Landman, U. Stabilized-Jellium Description of Neutral and Multiply Charged Fullerenes C^{x±} 60. *Chem. Phys. Lett.* **1994**, *217*, 175–185.
- (97) Yannouleas, C.; Landman, U. Electronic Shell Effects in Triaxially Deformed Metal Clusters: A Systematic Interpretation of Experimental Observations. *Phys. Rev. B: Condens. Matter Mater. Phys.* **1995**, *51*, 1902–1917.
- (98) Landman, U.; Luedtke, W. D.; Burnham, N. A.; Colton, R. J. Atomistic Mechanisms and Dynamics of Adhesion, Nanoindentation, and Fracture. *Science* **1990**, *248*, 454–461.
- (99) Landman, U.; Luedtke, W. D.; Salisbury, B. E.; Whetten, R. L. Reversible Manipulations of Room Temperature Mechanical and Quantum Transport Properties in Nanowire Junctions. *Phys. Rev. Lett.* **1996**, *77*, 1362–1365.
- (100) Landman, U.; Luedtke, W. D.; Gao, J. Atomic-Scale Issues in Tribology: Interfacial Junctions and Nano-elastohydrodynamics. *Langmuir* **1996**, *12*, 4514–4528.